Improvements in MLPG formulation for 3D wave interaction with fixed structures

Shagun Agarwal[a], V Sriram[a,*], Shiqiang Yan[b], K Murali[a]

[a]*Department of Ocean Engineering, Indian Institute of Technology Madras, India*
[b]*School of Mathematics, Computer Science and Engineering, City, University of London, United Kingdom*

Abstract

This paper presents new developments in meshless local Petrov-Galerkin with Rankine source (MLPG_R) particle based method for studying interaction of waves with fixed structures in a numerical wave-tank. A new 3D formulation of the Lagrangian flow problem for incompressible fluid with optimised solution strategy is presented. The pressure Poisson equation is solved in local weak-form with integration done semi-analytically using a new symmetric expression. The wave-generation is done using one-way coupling with a 2D fully-nonlinear potential theory based finite-element model. Further a simple identification method for free-surface particles is proposed, which is shown to work well in vicinity of the structure. The solid-wall boundary condition is treated using ghost and mirror particles for accurate calculation of gradients. The waterline on domain boundary faces is treated using a tangentially moving side-wall approach which makes this particle based scheme capable of capturing small amplitude waves and focusing waves. The paper briefly presents experimental setup used for studying the interaction of a fixed emergent cylinder with uni-directional regular and focusing waves in 3D. The numerical model is validated against results from this experiment. An analysis is conducted on parameters related to local integration domain, wave-making coupling algorithm, particle distribution and time-step. This work highlights the use of hybrid approach for efficient and accurate simulation of waves-structure interaction.

1. Introduction

Numerical wave-tanks are important tools in studying wave-transformation and their interaction with fixed and floating structures. With advancements in computational technology and a growing demand for efficient and accurate analysis tools in the industry, numerous methods have been developed using different numerical schemes to study the wave-structure interaction. The methods can be classified based on their

---

*Corresponding author
Email address:* `vsriram@iitm.ac.in` (V Sriram)

governing equations and their numerical method. Potential flow models in wave-hydrodynamics solve the Laplacian or the Boussinesq type equations and show excellent performance in capturing wave refraction, diffraction, wave-wave interaction and in replicating wave-generation as done in physical wave-tanks. The viscous flow models solve the Navier-Stokes equation or Lattice Boltzmann equations and are required for
10 problems involving wave-breaking, run-up, violent interaction of waves with a number of fixed and floating structures. These models are often computationally expensive, which limits their application in practical ocean engineering.

Mesh based numerical schemes such as finite difference method (FDM) [1], finite volume method (FVM) and finite-element method (FEM) have been applied successfully in single phase and multi-phase problems
15 over the last few decades. The popular open-source FVM fluid package OpenFOAM has seen rigorous development in wave generation, propagation and interaction with structures [2, 3]. Single phase BEM models [4, 5] and FEM models for potential flow such as QALE-FEM (quasi-arbitrary Lagrangian and Eulerian finite element method) [6] have shown promising results for 3D waves and their interaction with fixed and floating structures, with improvements in simulation of over-turning waves [7]. However, these
20 methods have severe limitations for problems involving free-surface flow over practical domain. A single phase model for wave simulation requires additional numerical treatment to compute violent and overturning waves. The multi-phase models require a free-surface tracking algorithm and fluid identification approaches, such as volume of fluid (VOF), to differential the phases. In order to minimise mass and momentum loss, the mesh needs to be of sufficient quality in every location where the free-surface may lie at any time-step.
25 These methods also need meshing of the air region in a two phase water-air interface problem, which may not be necessary for most ocean engineering free-surface problems. On adding a floating or fixed structure to this domain, an additional complexity is introduced. Earlier mesh based approaches relied on use of computationally costly methods such as adaptive meshing for ensuring a body-confirming mesh at every time-step. Advanced techniques have been developed for modelling complex and moving geometries in mesh-
30 based schemes. These include overset method [8] which consists of overlapping grids and can easily execute large motion of a body. Immersed boundary methods [9, 10] let go of the body-conforming mesh requirement, and instead modify the governing equation to incorporate a structure, thus modelling complex and moving geometries. Other such examples are Cartesian cut-cell method [11], partial cell treatment (PCT) [12] and virtual boundary force method [13]. A few examples of these mesh-based techniques applied to wave-
35 structure interaction are [14, 15, 13]. However, implementing boundary conditions in these techniques may require investigation of the conservation properties, and controlling the exact mesh size around the geometry may be a challenge.

Mesh-free methods provide a refreshed approach for modelling free-surface flow problems which has lead to an increasing focus on them in ocean engineering over the past two decades. In mesh-free methods the
40 domain is discretised using particles without a predefined mesh connectivity. The solution procedure does not require a mesh at any step. Instead, it uses the nodes within a sub-domain with appropriate shape functions to solve the differential equation. Therefore the mesh-free approach provides a large number of options in solution procedure, weak or strong form approach, use of various shape and trial functions, shape and size of the neighbouring sub-domain and free-surface particle identification methods. A popular example
45 is smoothed particle hydrodynamics method (SPH) [16, 17], which has shown good results for free-surface problems over the last decade. It solves the governing equation in strong form and uses smoothed kernel functions for calculating gradient. However, it usually requires large number of nodes and relies on GPU speed-up for practical run-times. Other popular schemes include moving particle semi-implicit method (MPS) [18, 19], particle finite element method (PFEM) [20] and meshless local Petrov-Galerkin method
50 (MLPG) [21]. A more recently developed scheme, called fragile point method (FPM) [22] uses simple local discontinuous trial and test functions for solving extreme problems such as rupture and fragmentation.

The current work is built up on the meshless local Petrov-Galerkin method with Rankine source function (MLPG_R) [23]. It solves the Navier-Stokes equation using the projection scheme, where only the pressure Poisson equation is solved in weak form. By using a continuous trial function in the weak form, the gradients
55 can be calculated using the trial function itself. The choice of Rankine source as the test function allows removal of gradient operators from the unknown variables to the known variables which enhances the stability of the solution. This method has been applied successfully in 2D for problems related to wave-breaking and

run-up [24] and recently for interaction with floating bodies [25].

This method, along with the other mentioned mesh-free schemes, provide solutions to the issues with the mesh-based schemes in free-surface flow problems. However their computational cost limits their application in large practical domains. The current work aims at targeting this problems with two approaches, a semi-analytical integration approach and hybrid modelling. We provide a method to evaluate the integrals in local weak form of the pressure Poisson equation using a semi-analytical technique with the quantification of the error term. We investigate the influence of the parametric radius in this integration scheme on the stability of the system. Using this technique we aim to reduce the time in assembling the system matrix and to reduce the iterations required for its solution.

The hybrid modelling approach in this work intends to use the advantages of potential flow models in wave generation, propagation and its transformation over large distances, where the viscosity conditions are not required. We provide the algorithm for transferring waves generated and propagated in a 2D fully non-linear potential theory (FNPT) model to this 3D MLPG_R model as a replacement for the wave-making boundary condition. The current state of such coupling between potential and viscous flow models was discussed in [24]. Thus by using the viscous model only in the vicinity of the structure, this hybrid approach can drastically reduce computational time and limit the numerical dissipation of the waves. This approach shows its benefits particularly in focusing wave problems, where the focusing point may lie far from the wave-paddle.

We have focused on improving the implementation of side-wall boundary condition to reduce the traditional wave-dissipation over long distances using a moving side-wall approach. This enables us to simulate small amplitude waves and hence allows accurate replication of focusing waves. This work also presents a free-surface particle detection method with improved performance especially in the wake of a structure under the action of incoming waves. We have also incorporated the recent developments in application of wall boundary condition on 3D structures inside the fluid domain, particle collision and wave-absorption.

The paper is organised with the description of the governing equations and the improved solution procedure. It discusses the one-way coupling algorithm with the 2D FNPT model, the free-surface identification method and the other improvements. The results provide a discussion on the integration domain radius. A detailed investigation is done on the influence of the overlapping zone in the coupling procedure for solitary, regular and focusing waves. This is followed by a brief description of the experimental set-up used for obtaining the data on interaction of fixed cylinder with regular and focusing waves. And finally the results obtained from this hybrid model on the same experiments are presented and validated against the physical data.

2. Formulation of the problem

2.1. Governing equations

The incompressible flow in the numerical wave tank with domain Ω bounded by boundary $\Gamma, t \geq 0$ and is governed by Lagrangian form of Navier-Stokes equations given by the conservation of mass Eq. (1a) and conservation of momentum Eq. (1b). The variable $\vec{u} = d\vec{r}/dt$ is velocity vector, $\vec{r}$ is the position vector, ρ is fluid density which is assumed to be constant, P is the local pressure, $\vec{g} = -9.81\hat{k}$ is body force vector and ν is the kinematic viscosity of the fluid.

$$\nabla.\vec{u} = 0 \qquad \text{in } \Omega \tag{1a}$$

$$\frac{D\vec{u}}{Dt} = \frac{-1}{\rho}\nabla P + \vec{g} + \nu\nabla^2\vec{u} \qquad \text{in } \Omega \tag{1b}$$

The numerical wave tank is spatially dicretised using particles. The boundary value problem is completed with three types of boundary conditions (BC), 1) Wave-maker Γ_a, 2) Free surface Γ_b, 3) Rigid wall Γ_c. The wave-maker boundary is implemented using a one-way coupling algorithm with a fully non-linear potential theory based finite element model on the boundary Γ_a and is described in detail in section 2.4. The free-surface BC requires identification of particles lying on the free surface, as described in section 2.5, and then

application of Dirichlet type condition of $P = P_{atm}$ at those nodes on the boundary Γ_b. The rigid wall BC is applied by assuming zero normal flow across the boundary Γ_c which gives the velocity condition as Eq. (2a), where $\vec{U}$ is velocity of the wall and $\vec{n}$ is its outward unit normal. Pressure BC for the wall is given by Eq. (2b), which is obtained by substituting Eq. (2a) in the scalar product of Eq. (1b) with $\vec{n}$. Here $\dot{\vec{U}}$ is acceleration of the wall.

$$\vec{u}.\vec{n} = \vec{U}.\vec{n} \qquad \text{on } \Gamma_c \tag{2a}$$

$$\vec{n}.\nabla P = \rho \left(\vec{n}.\vec{g} - \dot{\vec{U}}.\vec{n} + \vec{n}.(\nu\nabla^2\vec{u}) \right) \qquad \text{on } \Gamma_c \tag{2b}$$

The rigid-wall is treated as slip-wall BC because a no-slip BC would require accurate capturing of tangential gradient of velocity in close vicinity of the wall using appropriately fine node resolution, and is not an area of focus for this paper.

2.2. Solution procedure for governing equation

The system of governing equation in Eqs. (1) is solved using the projection scheme, in order to decouple the pressure gradient terms and to obtain a governing equation for pressure.

Step 1. Solve for intermediate velocity
An intermediate velocity $\vec{u}^*$ is calculated by removing the pressure gradient term from the momentum equation. The temporal derivative is expanded using Taylor series accurate till first order.

$$\vec{u}^* = \vec{u}^n + \Delta t \left(\vec{g} + \nu\nabla^2\vec{u}^n \right) \qquad \text{in } \Omega \tag{3}$$

Step 2. Solve for Pressure
The pressure governing equation is obtained by subtracting Eq. (3) from the momentum equation, taking the divergence of the resultant vector equation and substituting conservation of mass Eq. (1a) for velocity vectors $\vec{u}^n$ and $\vec{u}^{n+1}$.

$$\nabla^2 P^{n+1} = \frac{\rho}{dt}\nabla.\vec{u}^* \qquad \text{in } \Omega \tag{4a}$$

$$P^{n+1} = P_{atm} \qquad \text{on } \Gamma_b \tag{4b}$$

$$\vec{n}.\nabla P^{n+1} = \rho(\vec{n}.\vec{g} - \vec{n}.\dot{\vec{U}}^{n+1}) \qquad \text{on } \Gamma_c \tag{4c}$$

The above equation can be further modified by subtracting a linear quantity $P^* = \rho g(H_0 - z^n)$ from the instantaneous pressure P^{n+1} in Eq. (4). With the assumption of H_0 as constant, P^* satisfies $\nabla^2 P^* = 0$, and also simplifies the boundary condition at walls given that z is the vertical coordinate. H_0 is chosen as mean still water depth.

$$\nabla^2 q = \frac{\rho}{dt}\nabla.\vec{u}^* \qquad \text{in } \Omega \tag{5a}$$

$$q = P_{atm} - P^* \qquad \text{on } \Gamma_b \tag{5b}$$

$$\vec{n}.\nabla q = -\rho\vec{n}.\dot{\vec{U}}^{n+1} \qquad \text{on } \Gamma_c \tag{5c}$$

$$P^{n+1} = q + P^* \tag{5d}$$

The above modification allows for a faster convergence for the Poisson equation. The terms in P^* are known from previous time-step and therefore does not increase complexity of the process. In our numerical test case with identical set-up, the Poisson equation solved using bi-conjugate gradient stabilised method achieves convergence in 641 iteration for the original Poisson equation and 194 iterations for the modified Poisson equation.
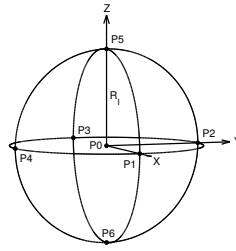
Figure 1: Schematic showing location of the integration points within the spherical sub-domain of radius R_I around a node

Step 3. Velocity correction and particle position update

The final velocity is then corrected using the intermediate velocity and the gradient of the pressure. After applying the boundary conditions for velocity, the particle position is updated using first order time-stepping.

$$\vec{u}^{n+1} = \vec{u}^* - \Delta t \frac{1}{\rho} \nabla P^{n+1} \qquad \text{in } \Omega \tag{6a}$$

$$\vec{n}.\vec{u}^{n+1} = \vec{n}.\vec{U}^{n+1} \qquad \text{on } \Gamma_c \tag{6b}$$

$$\vec{r}^{n+1} = \vec{r}^n + \vec{u}^{n+1}\Delta t \tag{6c}$$

In the above solution procedure Eq. (3) and Eqs. (6) are solved in 'strong' form with the gradients calculated using simplified finite-difference interpolation (SFDI) method as described in [26]. Pressure Poisson equation Eqs. (5) is solved in a 'weak' form to reduce the order of the equation. This procedure is a defining difference between the particle based schemes such as reproducing kernel particle method [27], element free Galerkin method [28] and smoothed particle hydrodynamics (SPH) [16]. In the present work, the equation is solved using meshless local Petrov-Galerkin method with Rankine source function (MLPG_R).

2.3. Weak-form solution using MLPG_R

The local weak form of pressure Poisson equation is evaluated at each node within a spherical sub-domain of radius R_I with the node as its centre. The 3D sub-domain is denoted by Ω_I with its surface boundary as Γ_I having outward unit normal $\vec{\lambda}$. Eq. (7) is the local weak form of Eq. (5a), where ψ is the test function.

$$\int_{\Omega_I} \psi \nabla^2 q \, d\Omega = \frac{\rho}{dt} \int_{\Omega_I} \psi \nabla.\vec{u}^* \, d\Omega \tag{7}$$

As shown in [29], the use of Rankine source function as the test function offers a few important simplifications for the pressure Poisson equation. It reduces the left-hand side from a domain to a surface integral. The Laplacian operator on the unknown quantity q is simplified to the gradient of the analytically known quantity ψ. On the right hand side too the gradient operator is shifted from the numerically calculated quantity $\vec{u}^*$ to analytically known quantity ψ. With the substitution of $\psi = \frac{1}{4\pi}(1 - R_I/r)$, where r is the distance between the centre of Ω_I and a location within Ω_I, Eq. (5a) is reduced to Eq. (8). The modified pressure equation Eq. (8) does not require numerical calculation of derivative of any quantity.

$$\int_{\Gamma_I} \vec{\lambda}.(q\nabla\psi) \, d\Gamma - R_I q = \frac{\rho}{\Delta t} \int_{\Omega_I} \vec{u}^*.\nabla\psi \, d\Omega \tag{8}$$

The calculation of domain and surface integrals within the spherical sub-domain around the node is done using a semi-analytical method. This approach is a further development on the work in [23]. The earlier derivation relies on dividing the sphere into eight divisions and assuming a linear variation of variables within each division for domain integral, and a linear variation along the surface of each division for a surface integral. The resultant expression is asymmetric in space and does not provide with the order of

155 error. We have done an alternate derivation using the complete Taylor series expansion and then chose to terminate final expression based on an acceptable order of error.

$$\frac{1}{4\pi} \int_0^{2\pi} \int_0^{\pi} q \sin(\theta)\, d\theta\, d\gamma - q = \frac{1}{4\pi} \frac{\rho}{\Delta t} \int_0^{R_I} \int_0^{2\pi} \int_0^{\pi} u_r^* \sin(\theta)\, d\theta\, d\gamma\, dr \tag{9}$$

On substituting the expression for Rankine source function as ψ in Eq. (8) and dividing the resultant by the constant R_I, we obtain Eq. (9) with integrals in spherical coordinate, where u_r^* is the radial intermediate velocity. On expanding variables q and velocity components $\vec{u} = (u, v, w)$ about the centre of the spherical
160 sub-domain in 3D using Taylor series expansion and integrating the final expression analytically, the integrals in Eq. (9) result to Eq. (10), which is expanded till $(R_I)^4$. Here q_0, u_0, v_0, w_0 are variables at the centre of the spherical sub-domain.

$$\begin{aligned}
\int_0^{2\pi} \int_0^{\pi} q \sin(\theta)\, d\theta\, d\gamma = {}& 4\pi q_0 + \frac{2}{3}\pi R_I^2 (q_{0,xx} + q_{0,yy} + q_{0,zz}) \\
& + \frac{1}{30}\pi R_I^4 (q_{0,xxxx} + q_{0,yyyy} + q_{0,zzzz}) \\
& + \frac{1}{30}\pi R_I^4 (q_{0,xxzz} + q_{0,xxzz} + q_{0,yyzz}) + ...
\end{aligned} \tag{10a}$$

$$\begin{aligned}
\int_0^{R_I} \int_0^{2\pi} \int_0^{\pi} u_r^* \sin(\theta)\, d\theta\, d\gamma\, dr = {}& \frac{2}{3}\pi R_I^2 \left(u_{0,x}^* + v_{0,y}^* + w_{0,z}^* \right) \\
& + \frac{1}{30}\pi R_I^4 \left(u_{0,xxx}^* + u_{0,xyy}^* + u_{0,xzz}^* \right) \\
& + \frac{1}{30}\pi R_I^4 \left(v_{0,xxy}^* + v_{0,yyy}^* + v_{0,yzz}^* \right) \\
& + \frac{1}{30}\pi R_I^4 \left(w_{0,xxz}^* + w_{0,yyz}^* + w_{0,zzz}^* \right) + ...
\end{aligned} \tag{10b}$$

The expressions for the integrals involve no numerical approximations so far. In our work we will terminate
165 the expressions till $(R_I)^3$ giving us the integration error proportional to $(R_I)^4$. The first and second order derivatives of variables about the centre of the spherical sub-domain can be numerically estimated using central difference scheme using values at the points at distance R_I along the axes of the sphere as shown in Fig. (1). The resultant expressions are symmetric along the 3 axes with a leading error term proportional to R_I^4 and require only 6 integration points.

$$\begin{aligned}
\int_0^{2\pi} \int_0^{\pi} q \sin(\theta)\, d\theta\, d\gamma &= \frac{2}{3}\pi R_I^2 \left(\frac{q_1 + q_2 + q_3 + q_4 + q_5 + q_6}{R_I^2} + E(R_I^2) \right) + E(R_I^4) \\
&= \frac{2}{3}\pi \left(q_1 + q_2 + q_3 + q_4 + q_5 + q_6 \right) + E(R_I^4)
\end{aligned} \tag{11a}$$

170

$$\int_0^{R_I} \int_0^{2\pi} \int_0^{\pi} u_r^* \sin(\theta)\, d\theta\, d\gamma\, dr = \frac{1}{3}\pi R_I \left(u_1^* - u_3^* + v_2^* - v_4^* + w_5^* - w_6^* \right) + E(R_I^4) \tag{11b}$$

The integrated expressions are now substituted in Eq. (9) to give the final form of the pressure Poisson equation, Eq. (12), with leading error proportional to R_I^4. The choice of R_I therefore is an important parameter in determining the accuracy and convergence rate for the solution. In the section 3.1, we have investigated the influence of increasing R_I on the solution and have prescribed an appropriate value for our
175 set of simulations.

$$\frac{1}{6} \left(q_1 + q_2 + q_3 + q_4 + q_5 + q_6 \right) - q_0 = \frac{\rho}{\Delta t} \frac{R_I}{12} \left(u_1^* - u_3^* + v_2^* - v_4^* + w_5^* - w_6^* \right) \tag{12}$$

The value of variables at integration points is evaluated using the moving least-squares shape function (MLS), [30, Ch. 3]. Hence with the interpolation as $q(\vec{r}) = \sum_{k=1}^{M} \Phi_k q_k$, where M is the number of neighbouring nodes and Φ is the MLS shape function, the weak form of pressure Poisson equation for domain with N nodes is converted to system of N linear equations given by $[A]_{N \times N}[q]_{N \times 1} = [B]_{N \times 1}$, where

$$A_{jk} = \begin{cases} \frac{1}{4\pi} \int_0^{2\pi} \int_0^{\pi} \Phi_k(x) \sin(\theta) \, d\theta \, d\gamma - \Phi_k(x_j) & \text{for interior} \\[2ex] \vec{n}.\nabla \Phi_k(x_j) & \text{for } \Gamma_c \end{cases} \tag{13a}$$

$$B_j = \begin{cases} \frac{1}{4\pi} \frac{\rho}{\Delta t} \int_0^{R_I} \int_0^{2\pi} \int_0^{\pi} u_r^* \sin(\theta) \, d\theta \, d\gamma \, dr & \text{for interior} \\[2ex] -\rho \vec{n}.\dot{\vec{U}} & \text{for } \Gamma_c \end{cases} \tag{13b}$$

The gradient for applying the wall boundary condition in the above system is calculated using SFDI [26]. In our work the system of linear equations is solved using bi-conjugate gradient stabilised method (BiCGStab) and generalised minimal residual method (GMRES). They are provided by an open-source OpenMP enabled Paralution library [31]. The comparison between the rate of convergence and the total parallel scalability for our code is presented in section 3.1.

2.4. One-way coupling with FNPT-FEM

The Lagrangian model allows generation of waves in a numerical wave-tank (NWT) by directly modelling the motion of the wave-maker. It is a convenient approach that allows duplicating the exact piston motion of physical wave tank. However in order to achieve a stable wave-train, the structure under study should be placed multiple wave-lengths away from the wave-maker. The flow under the waves during this propagation phase is potential flow, therefore using a 3D viscous model just for wave-generation and propagation would be computationally costlier and will invariably lead to numerical dissipation. This problem is further compounded in focused wave studies where the focusing point may be at a significant distance from the wave-maker. Alternatively, theoretical source function can be used to generate the waves starting near the structure itself. This can reduce the domain size, and thus reduce computational cost, however the theoretical functions will not be fully nonlinear and involve approximations that limit the wave height and steepness. In focused wave studies these limitations can lead to generation of spurious sub and super harmonics in the numerical wave-tank [32].

In our work we use a 2D finite element model for fully nonlinear potential theory (FNPT-FEM) for wave-generation and its propagation for majority of the distance between the wave-maker and the structure. It is a proven model with excellent correlation with experiments as shown in [32]. Thereafter the wave is transferred from FNPT-FEM to MLPG_R near the structure using a one-way coupling algorithm. It allows us to retain the nonlinear wave-trains without significant numerical losses and also reduced computational effort by limiting the domain requirement for 3D MLPG_R to only near the structure. In principle one can employ a 3D FNPT model [7] instead. Currently we have only presented uni-directional waves for which the 2D model is sufficient, however our future work will be coupling with a 3D model to simulate
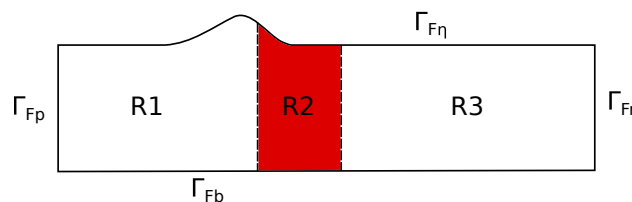

Figure 2: Schematic for the FNPT-FEM domain with coloured region indicating the region from where data is passed to MLPG_R
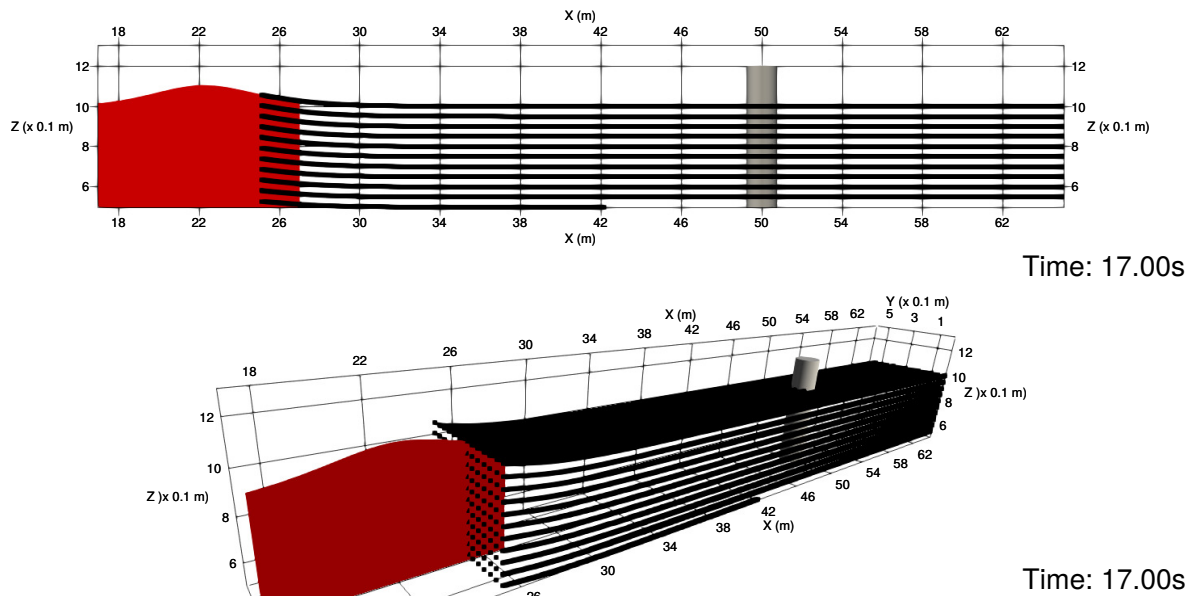
Figure 3: FNPT-FEM sub-domain $R2$ in 2D shown in red, overlapping with part of MLPG_R domain in 3D

multi-directional waves, and to shift the sponge layer in the downstream region to 3D FNPT.

$$\frac{\partial \phi}{\partial x} = \dot{x}_p(t) \qquad\qquad \text{at } x = x_p(t) \text{ on } \Gamma_{Fp} \tag{14a}$$

$$\frac{\partial \phi}{\partial n} = 0 \qquad\qquad \text{on } \Gamma_{Fb} \text{ and } \Gamma_{Fr} \tag{14b}$$

$$\frac{\partial \phi}{\partial t} = g\eta - \frac{1}{2}\nabla\phi\nabla\phi \qquad \text{on } \Gamma_{F\eta} \tag{14c}$$

FNPT-FEM is a 2D semi-Lagrangian model in X-Z plane, where the nodes are allowed to move in vertical direction to model free-surface movement. The flow is assumed to be incompressible and irrotational and hence viscous forces are neglected. Governing equation for the velocity potential ϕ is $\nabla^2\phi = 0$, where $\vec{u} = \nabla\phi$. Vertical left boundary Γ_{Fp} of the 2D domain is wave-maker, with the Neumann boundary condition enforced by Eq. (14a), where $\dot{x}_p$ is velocity of the piston type wave-paddle. Bottom Γ_{Fb} and right Γ_{Fr} edges have wall boundary condition applied using Eq. (14b). With the assumption of non-breaking waves, non-linear dynamic free-surface boundary condition is applied at the continuous free surface $\Gamma_{F\eta}$ using Eq. (14c), obtained using the unsteady Bernoulli equation. Here η is the surface elevation from initial still-water level. The wave paddle motion is calculated from piston-type wave-maker theory with second order correction based on [33]. The detailed formulation and validation for this model is given in [34].

The complete FNPT-FEM domain, as shown in Fig. (2), contains three regions of interest. In $R1$ waves are generated and allowed to propagate till they reach the vicinity of the MLPG_R domain. $R2$ is the region overlapping with the 3D MLPG_R domain as shown in Fig. (3). Particle position, velocity and pressure are transferred from this region to MLPG_R nodes. $R3$ is a redundant region with the function of avoiding reflection within the FNPT domain by using a large sponge layer. Given that FNPT-FEM is a 2D potential flow code, we use a long $R3$ to avoid any reflection at extremely low computational cost.

The coupling procedure within the MLPG_R domain is limited to only a few nodes inside the FNPT-FEM overlapping region. As the FNPT-FEM domain is 2D, the data from this model is assumed to have zero variation of variables along the y-axis. The one-way coupling procedure is described below.

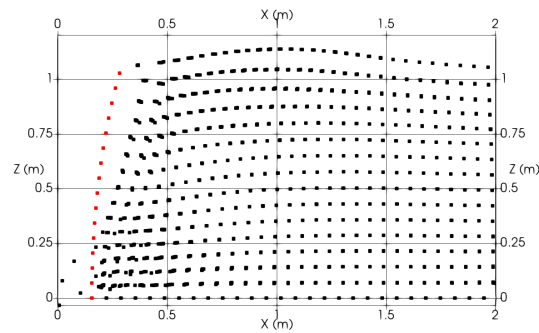Step 1 : Extract data from time-step (n+1) from FNPT-FEM inside $R2$

Figure 4: Internal fluid nodes (in black) leaking through the left face nodes (in red) when coupling zone is not used within MLPG_R domain

Step 2 : Interpolate the variables in MLPG_R domain at particle position $\vec{r}^n$ using MLS with surrounding FNPT nodes to give the values $V_{int}^{n+1}(\vec{r}^n)$, consistent with Eq. (6c). Here V represents the variables P, $\vec{u} = (u, v, w)$.

Step 3 : The extracted values $P_{int}^{n+1}(\vec{r}^n)$ at the left face of MLPG_R domain are used to calculate $q_{int}^{n+1}(\vec{r}^n) = P_{int}^{n+1}(\vec{r}^n) - \rho P^*$. These values are then used to apply Dirichlet type BC on the left face for the pressure Poisson equation Eq. (5a).

Step 4 : Finally, before the position update step Eq. (6c), the values of P, $\vec{u} = (u, v, w)$ within the overlapping nodes of MLPG_R domain are corrected to gradually merge with the FNPT-FEM solution using Eq. (15).

$$V^{n+1}(\vec{r}^n) = \alpha V_{int}^{n+1}(\vec{r}^n) + (1 - \alpha)V_{ML}^{n+1}(\vec{r}^n) \tag{15a}$$

$$\alpha = 1 - 3\left(\frac{x^0 - x_L^0}{L_c}\right)^2 + 2\left(\frac{x^0 - x_L^0}{L_c}\right)^3 \tag{15b}$$

Here α is the coupling coefficient which has to be calculated only based on the position of MLPG_R particles at zeroth time-step. x_L^0 is the left-most position at zeroth time-step and L_c is the length of the coupling region within MLPG_R domain. Hence the value of α does not change with time and therefore does not require any additional computation. As per our study it is necessary to use at-least a minimum coupling region within MLPG_R. Applying just the Dirichlet boundary condition with known values from FNPT-FEM on the left face without the use of a overlapping zone will lead to leak of internal fluid nodes through the left face as shown in Fig. (4). This is because the left face is not a wall boundary. In section 3.2 we have studied the required L_c for transferring solitary, regular and focused wave-train from FNPT-FEM to MLPG_R.

2.5. Identification of free-surface

Application of free-surface BC, Eq. (5b), in pressure Poisson equation requires accurate detection of the free-surface nodes. A misidentification of fluid node as free-surface can create artificial sharp gradients and noise in pressure values. Many of the free-surface identification algorithms rely on particle number density [35, 19]. This method uses the variation of instantaneous particle number density as compared with zeroth time-step value for identifying free-surface nodes. This approach was used in earlier MLPG work for successfully simulating 3D breaking waves as shown in [23]. However this approach is difficult to implement when the domain has variable particles number density. In the vicinity of structures, particles have a tendency to collate or disperse creating regions of high and low particle number density with respect to the zeroth time-step, which can lead to misidentification of fluid nodes as free-surface. The sequence of images in Fig. (5) show a few instances of this error inside the fluid domain under a steep wave and in the vicinity of the cylinder during their interaction. This error results in artificial spikes in the numerical
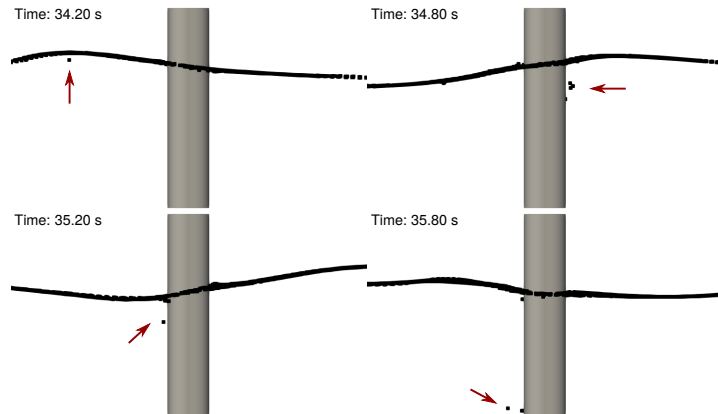
Figure 5: Sequence of snapshots showing the misidentification of free-surface nodes inside the fluid domain as indicated by the red arrow
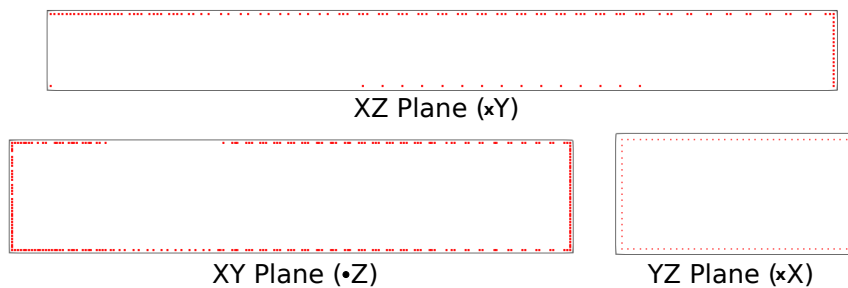

Figure 6: The summated unit displacement vector method without ghost nodes detects the fluid nodes near corners of the domain as free-surface as shown in red

pressure results and can lead to masking of a physical phenomenon. For example, the ringing of vertical cylinders under certain waves could get masked within the noise of such errors. It can also create artificially high gradients causing fluid particles to shoot out of the domain and can result in failure of the simulation. Therefore there is a need to develop free-surface identification techniques which are not directly dependent on the particle number density.

We propose a simple free-surface detection method. For a node i a summated unit displacement vector $\vec{v}_i$ is calculated as shown in Eq. (16). Here R_f is a size of a spherical sub-domain around node i, calculated using M closest neighbours. If $|\vec{v}_i| > v_{max}$ then the node is on free-surface. In our work we have used $M = 6$, $\beta = 2.0$ and $v_{max} = 0.24$. This approach alone however will identify nodes near corners and faces of the domain as free-surface as shown in Fig. (6). In order to solve this we add a single layer of ghost nodes along the outward normal of the side, bottom and body faces, placed at a distance of $0.55R_f$. In case of highly irregular node distribution, two or more layers of ghost nodes along the outward normal can be used. This approach eliminates the misidentification problem for the free-surface nodes as shown in Fig. (7).

$$\vec{v}_i = \sum_k \frac{\vec{r}_{ik}}{|\vec{r}_{ik}|} \qquad \text{for } |\vec{r}_{ik}| \leq R_f \tag{16a}$$

$$R_f = \frac{\beta}{M} \sum_{k=1}^{M} |\vec{r}_{ik}| \tag{16b}$$

2.6. Treatment of the tangentially moving side-wall boundary

Identification and treatment of waterline on the domain boundaries is crucial for wave propagation. In a 2D domain the waterline is only limited to a point on each face and a simple numerical treatment through
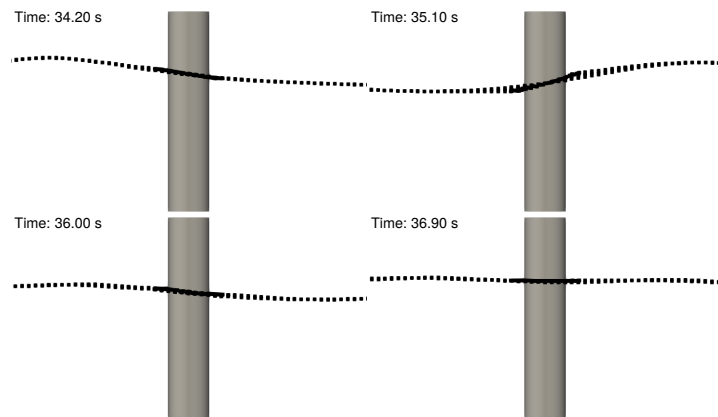
Figure 7: Sequence of snapshots showing the free-surface under a steep focusing wave interacting with a cylinder with no falsely identified free-surface nodes
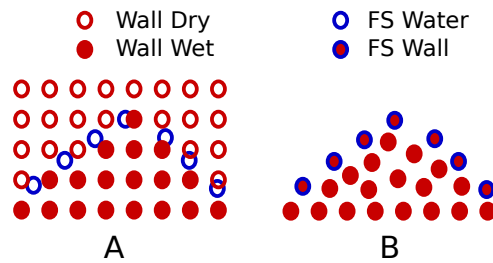

Figure 8: Schematics for two approaches for treating waterline on side-walls of the domain

interpolation is sufficient. In a 3D domain the waterline extends over the entire length. Fig. (8) shows the possible approaches for treating the waterline. The approach A is a conventional wet-dry approach where the side wall particles are fixed and are identified to be under the fluid (wet) by the neighbouring fluid free surface. As shown from the schematic, this approach leads to a "stepped" waterline, thus requiring high density particle distribution near side-wall and making it unsuitable for small amplitude waves. These waves are crucial for generating high steepness focusing waves whose interaction with structures is an important study case.

This work has implemented a tangentially moving wall approach B on the vertical faces of the domain. The side wall particles are moved as per Lagrangian motion Eq. (6c). The boundary condition on these side wall particles is slip-wall with no normal flow across the face. As per Eq. (4c) reducing to $\vec{n}.\Delta P = 0$, the gradient of pressure in the velocity correction steps can be limited to just the respective vertical plane (XZ or YZ) for these vertical faces. Hence by converting the gradient from 3D to 2D at the waterline the associated error due to incomplete surrounding domain can be reduced. This along with the now continuous waterline as shown in Fig. (8) makes the approach suitable for both small and large amplitude waves, which is crucial for replicating the focusing wave test cases. This method however needs to be further tested for 3D breaking waves, where the purely Lagrangian motion of the particle may introduce problems. Additionally, if the viscous effects on this domain side-wall are of significance for a particular problem, then the boundary condition has to be modified to no-slip type, for which the boundary particle velocity is zero. In such a case, the moving side wall approach will not be suitable.

2.7. Implementation of rigid wall boundary condition

The rigid wall BC for pressure and velocity are given by Eq.(4c) and Eq.(6c). The boundary condition is directly applied as Neumann type BC while solving the weak form of the pressure Poisson equation as described in Eqs.(5). However, the velocity correction step is solved in 'strong' form and it will require special
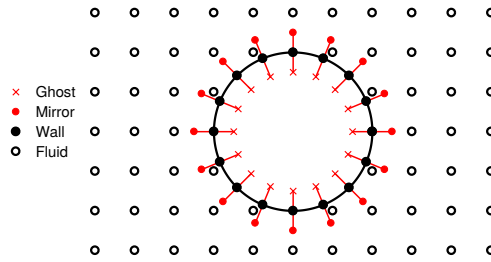
Figure 9: The ghost particle (G, red star) and mirror particle (M, red dot) placed around the corresponding wall particle (W) for applying rigid wall boundary conditions
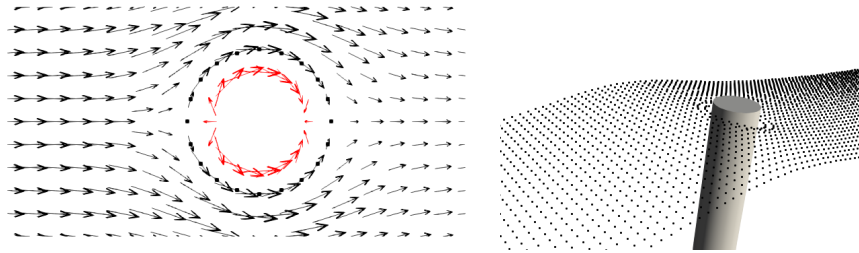

Figure 10: Top view of velocity vector at ghost nodes (in red), wall nodes (in black + ●) and fluid nodes (in black) for applying slip velocity boundary condition for cylinder under the crest of a wave

treatment for accurately applying the pressure and velocity BC. We achieve this using pairs of mirror M and ghost G particles attached to every wall node W as shown in Fig. (9). The two points are placed along the outward unit normal $\vec{n}$ of the wall point W at a distance of l_G, on opposite sides of the wall point, $\vec{r}_G = \vec{r}_W + \vec{n}\,l_G$ and $\vec{r}_M = \vec{r}_W - \vec{n}\,l_G$. The mirror point M should be within the fluid domain and the values of pressure and velocity are interpolated at this point using the surrounding fluid nodes with MLS. As the wall point is the midpoint between M and G, the values of pressure and velocity at G are evaluated using Eqs.(17) in order to apply the boundary conditions at the corresponding wall point W. Here ρ is fluid density, $\vec{\tau}_1$ and $\vec{\tau}_2$ are the corresponding tangents to the normal $\vec{n}$, and $\vec{U}_W = (U_W, V_W, W_W)$ is the required velocity boundary condition at W. Fig. (10) shows an example of the velocity vector for the ghost nodes used to apply the slip velocity boundary condition at a stationary cylinder boundary under a wave-crest.

$$P_G = P_M + 2\rho\,l_G \left(\vec{n}.\vec{g} - \vec{n}.\dot{\vec{U}}_W^{n+1} \right) \tag{17a}$$

$$\begin{bmatrix} u_G \\ v_G \\ w_G \end{bmatrix} = \begin{bmatrix} n_x & \tau_{1x} & \tau_{2x} \\ n_y & \tau_{1y} & \tau_{2y} \\ n_z & \tau_{1z} & \tau_{2y} \end{bmatrix} \left(\begin{bmatrix} -n_x & -n_y & -n_z \\ \tau_{1x} & \tau_{1y} & \tau_{1z} \\ \tau_{2x} & \tau_{2y} & \tau_{2z} \end{bmatrix} \begin{bmatrix} u_M \\ v_M \\ w_M \end{bmatrix} + \begin{bmatrix} n_x & n_y & n_z \\ 0 & 0 & 0 \\ 0 & 0 & 0 \end{bmatrix} \begin{bmatrix} 2U_W \\ 2V_W \\ 2W_W \end{bmatrix} \right) \tag{17b}$$

2.8. Particle distribution and wave absorption

The fluid particles have a tendency to collate together or disperse in regions around a structure. This is a major issue for incompressible Lagrangian models. If two particle are too close to each other then, when compared with the sub-domain radius; the system of linear equations Eqs. (13) will not be solvable due to the matrix $[A]$ close to being singular. Conversely, if nodes drift too far apart then there will not be enough neighbours in the sub-domain to accurately apply MLS and SFDI. Most particle based models use techniques for correcting the distribution of particles. One example in assuming pseudo-compressible fluid by applying additional correction term in pressure Poisson equation based on particle number density [19]. Multiple versions of particle shifting techniques are also used to slowly nudge the particles in desired distribution [36]. In our work we have used a particle-collision algorithm as described in [37] based on kinetic collision
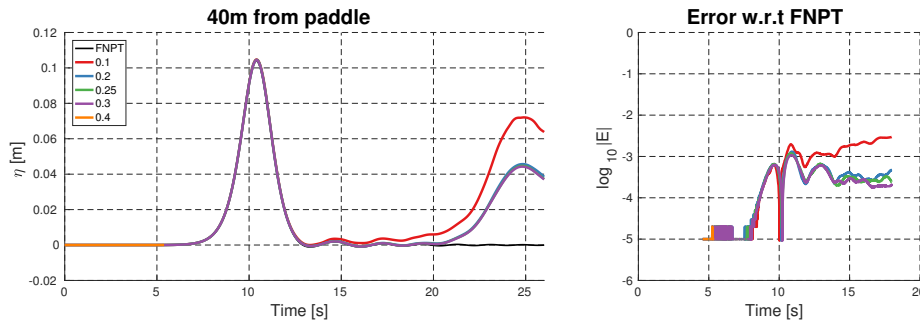
Figure 11: Surface elevation at $x = 40m$ for different values of α coefficient

theory. We assume a fully elastic collision between fluid particles, which ensure conservation of momentum and energy. The mass of wall particles within the collision algorithm is assumed to be very large with respect to the fluid nodes. This reduces the leak through walls as presented in the reference. Additionally,
320 we do a periodic re-distribution of all particles in the domain. In SPH model a similar re-distribution was successfully implemented in [38]. In 3D free-surface flows, this would first require an accurate mapping of the free surface, followed by distribution of nodes under this free-surface and the final interpolation of values using the 3D MLS interpolation with Gaussian weight function.

A sponge layer is placed on far-end of the domain to absorb the incoming waves. It is necessary for
325 studying the structure's interaction with regular and focused waves while keeping a limited domain size. The sponge layer is applied by using damping source term $S\vec{u}$ in the momentum equation. Here $S(x)$ is the power damping function of order n_S, as tested in [39] for SPH, x_0 and x_{max} are the beginning and end of the sponge layer zone. Thus resultant velocity vector obtained after the correction step will be modified to Eq. (18c). We have used $n_S = 3$ and $S_{max} = 10$ based on our own tests and the recommendations in [39].

$$\frac{D\vec{u}}{Dt} = \frac{-1}{\rho}\nabla P + \vec{g} + \nu\nabla^2\vec{u} - S\vec{u} \qquad \text{in } \Omega \tag{18a}$$

$$S(x) = S_{max}\left(\frac{x - x_0}{x_{max} - x_0}\right)^{n_S} \tag{18b}$$

$$\vec{u}^{n+1} = \frac{1}{1 + \Delta t S}\left(\vec{u}^* - \Delta t\frac{1}{\rho}\nabla P^{n+1}\right) \qquad \text{in } \Omega \tag{18c}$$

330 The developments in this paper, including the 3D formulation with new symmetric integration expression, new free-surface particle detection, side wall and rigid-wall treatment, and particle distribution are collectively named as meshless local Petrov-Galerkin method with Rankine source symmetric (MLPG_RS) to differentiate from [23].

3. Results and Discussions

335 *3.1. Influence of size of integration sphere on convergence*

In section 2.3 we have derived the semi-analytical technique for integration in the sub-domain around a node to evaluate the local weak form of the pressure Poisson equation. The resultant error is found to be proportional to R_I^4, where R_I is the radius of the spherical integration domain. We define R_I as given in Eq. (19), with $M = 6$ closest neighbours. The value of coefficient α is varied between 0.1 and 0.4 to check
340 the influence of increasing R_I on the converge of Poisson equation solver and on the accuracy of result.

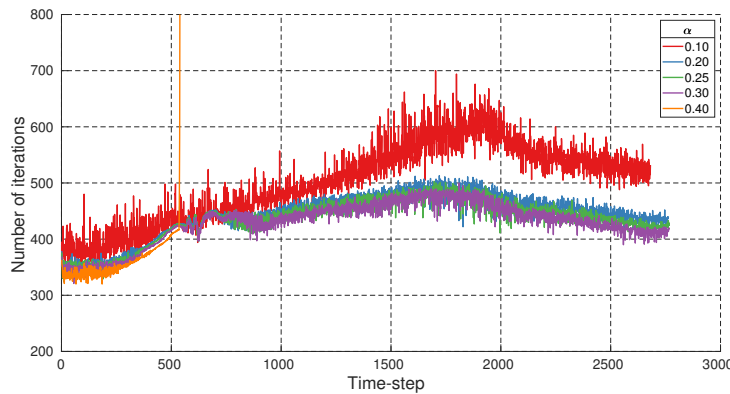$$R_I = \frac{\alpha}{M}\sum_{k=1}^{M}|\vec{r}_{ik}| \tag{19}$$

Figure 12: Number of iterations required by GMRES solver to reach the error limit at each time-step for different values of α coefficient
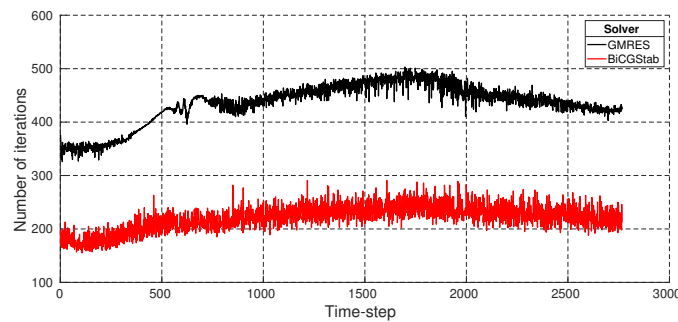

Figure 13: Comparison between number of iterations required by BiCGStab and GMRES solvers for identical test case

We investigate this using a test case with 65m long computational domain in which a solitary wave of height 0.1m is generated in water-depth of 1m. The wave is transferred from FNPT-FEM to MLPG_RS at 25m. Thus, the MLPG_RS domain is 40m long, starting from $x = 25$m till $x = 60$m and is filled with 218673 particles initially distributed at 0.05m. With the time-step of 0.01s, about 2700 time-steps in MLPG_RS give us the required results for comparison. A sponge layer of 8m is placed in the right end. Every setting for the simulation, including the size of neighbour domain for MLS interpolations, are kept identical in all cases, except for the value of α. A wave probe is kept at $x = 40$m to compare the results of MLPG_RS for different values of α with FNPT-FEM simulation, as shown in Fig. (11). Here the MLPG_RS solutions show partial reflection after 20s from the sponge layer due to the restriction of the domain size. Fig. (12) shows the comparison of the number of iterations requires by a GMRES solver to reach an error limit of 10^{-10} for different values of α. A large value of R_I leads to divergence of result due to the integration error being proportional to R_I^4 as shown by $\alpha = 0.4$. However a very small value of R_I ,as shown by $\alpha = 0.1$, requires larger number of iterations to achieve the solution and the wave probe reading does not correlate with the FNPT-FEM solution as seen in Fig. (11). Due to a smaller integration domain, the solution at a node is not linked with sufficient number of surrounding nodes, which is required in a local weak-form solution. This influences the condition number of the system making in more sensitive to the truncation errors, which explains the erratic number of iterations in Fig. (12) and divergence from the converged result in Fig. (11). The values of α between 0.2 and 0.3 show similar convergence and wave probe solution. The method shows an inverted bell curve type dependence on R_I, without being over-sensitive to its value. In our work, we have taken $\alpha = 0.25$.

We have tested same solitary wave test case with $\alpha = 0.25$ with solution obtained using BiCGStab
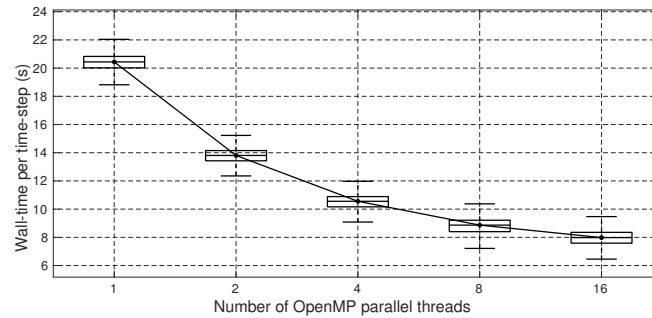
Figure 14: Boxplot showing speed scalability of the OpenMP parallelised code for different number of CPUs. The line plot is for the median wall-time per time-step

solver. Fig. (13) shows comparison between GMRES and BiCGStab solvers for identical test case with the error limit of 10^{-10}. BiCGStab requires half the number of iterations and hence saves computational time, however we have observed that it fails to converge in certain circumstances, especially near the beginning
365 of the simulation. Therefore we use BiCGStab as default solver and shift to GMRES if it fails to converge. The code has been made parallel using OpenMP and the Fig. (14) shows the time taken per time-step for the same solitary wave test case with 218673 nodes for different number of cores to test the scalability of the code. The tests were done on Intel Xeon E5-2640 v3 processor with clock speed of 2.60GHz. The authors do recognise recent works on GPU parallelisation of SPH [17], but it has not been focus of this work. In the
370 current state, about 75% of the code in made parallel using OpenMP, which entails a maximum speedup of 4x compared to a serial run. Further improvements can be made in simulation time by increasing the parallel portion, shifting from shared memory to distributed memory form, using a better sparse matrix solver and by moving parts of computation to GPU.

3.2. One-way coupling with FNPT for wave-generation

375   In section 2.4 we have described the procedure for one-way coupling of MLPG_RS with FNPT-FEM, where the waves are generated in FNPT-FEM using a piston-type wave-maker and are transferred to MLGP_R near the body using an overlapping zone of length L_c. In this section, we will investigate the influence of L_c and validate the coupling procedure.

3.2.1. Solitary Wave

380   The tests are first conducted for transfer of solitary wave. The 2D FNPT domain is 100m long and 1m deep. The mesh resolution is set to $\Delta x = 0.0625$m and Δy varying exponentially from 0.1094m near bottom to 0.0241m near the free-surface in 20 intervals. These mesh parameters are as per the recommendations in [34] and will not be investigated in this work. The region $R2$ of this domain as described in Fig. (2) is set from 24.5m to 34.5m with solution saved at a regular resolution of 0.05m at every time-step for coupling
385 procedure.The simulation time-step is set to 0.01s. A solitary wave of height 0.1044m is generated.

    The 3D MLPG_RS domain is initially a cuboid of length 40m, width 0.6m and depth 1m with a particle distribution done at regular intervals of 0.05m. It starts from 25m and goes till 65m with the left face within the $R2$ region of FNPT domain. A sponge layer of 10m is placed from 55m to 65m. The transfer of solitary wave is tested by comparing the wave probes at 30m and 40m in the FNPT domain and the coupled
390 FNPT+MLPG_RS domain. With the overlapping zone $L_c = 0.5$m, initially between 25m and 25.5m in the MLPG_RS domain, the wave probe comparison as shown in Fig. (15) demonstrates the successful transfer of solitary wave from FNPT domain to the MLPG_RS domain. As mentioned in section 2.4, the MLPG_RS particles in overlapping zone are identified only based on initial domain, after which their coupling weight is not modified. The MLPG_RS results beyond 40s shows the partial reflection of the solitary wave from the
395 sponge layer because a solitary wave would require very long sponge layers for a complete absorption. This is not visible in the FNPT domain because the domain length is set to a larger value in the FNPT domain.
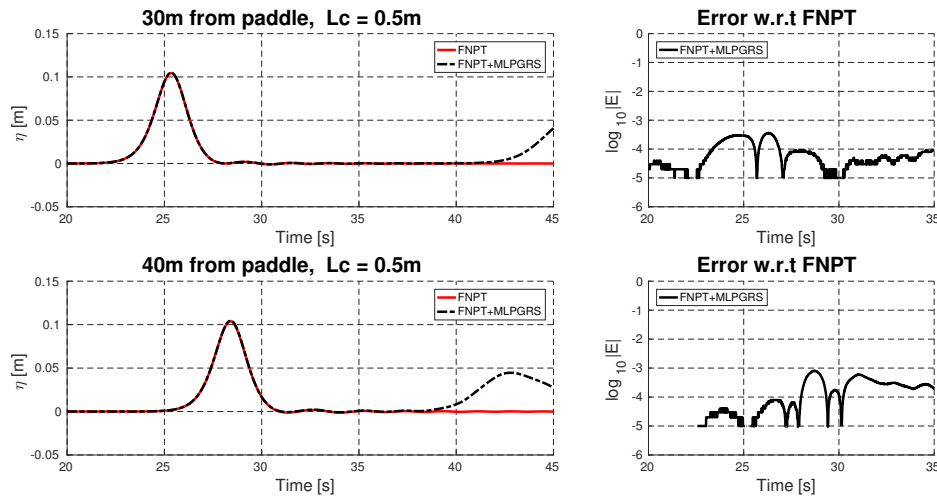
Figure 15: Wave probes comparison of surface elevation η between FNPT results and coupled FNPT+MLPG_RS results with $L_c = 0.5$m for solitary wave
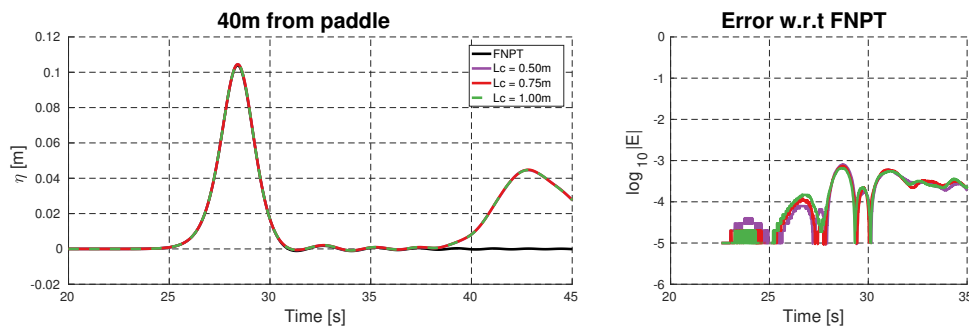

Figure 16: Wave probes comparison of surface elevation η between FNPT results and coupled FNPT+MLPG_RS results with different lengths of the overlapping zone for solitary wave

We can also observe the MLPG_RS results not showing dissipation of the solitary wave amplitude over the 15m of propagation shown in these figures, thus indicating low numerical errors.

The influence of L_c on the coupling is investigated by testing cases with identical setup for values of $L_c = 0.20$m, 0.30m, 0.40m, 0.75m, 1.00m. The coupling procedure fails for values of $L_c \leq 0.3$m due to leakage of fluid particles through the left face as was shown in Fig. (4). However for values $L_c \geq 0.5$m the results of the transfer of the wave are identical, as shown in Fig. (16). In each of these simulations, the log of relative error is less than -3 as shown in Fig. (15) and Fig. (16).

3.2.2. Regular and Focused Wave

The mesh and time-step setup as described under the solitary wave case was used to test the transfer of the regular wave $TW1$ and the focused wave $TW2$ from FNPT-FEM to MLPG_RS. The theoretical wavelength for the regular wave $TW1$ based on the dispersion relationship is 6.60521m. The overlapping zone length of $L_c = 0.50$m and 0.75m were tested, with the two cases having wave-probe readings comparable to FNPT as shown in Fig. (17). The final test was conducted for the focusing wave $TW2$ using a overlapping zone of length $L_c = 0.5$m. The resultant wave-probe readings at 30m and 40m as in Fig. (18) show agreeable comparison the FNPT-FEM result.

From these tests we can conclude that the one-way coupling for transfer of solitary, regular and focused waves from 2D FNPT-FEM to 3D MLPG_RS can be achieved using the algorithm described in this work.
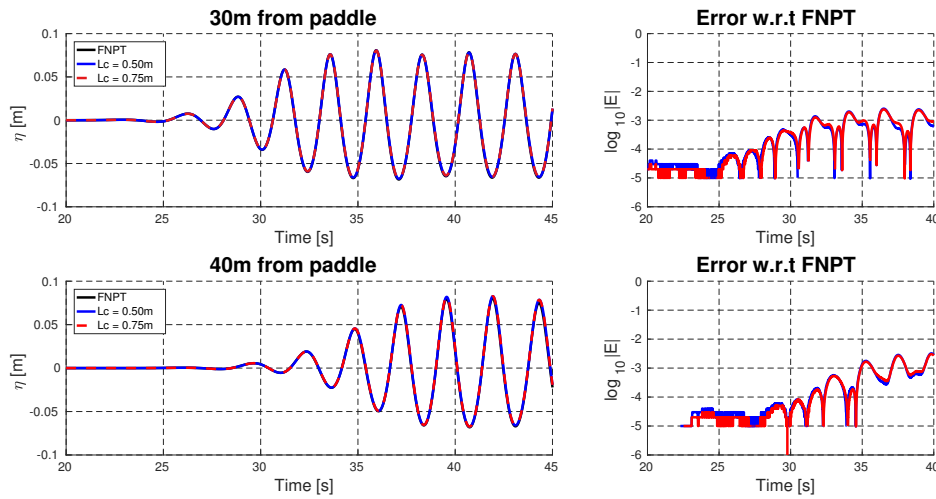
Figure 17: Wave probes comparison of surface elevation η between FNPT results and coupled FNPT+MLPG_RS results with different lengths of the overlapping zone for regular wave

A sufficient length of the overlapping zone in MLPG_RS domain is required to avoid the leakage of fluid particles through the left face. The length does not depend upon the type of the wave because $L_c \geq 0.50$m provided agreeable results for solitary, regular and focused. For the focusing wave case, where the theoretical wave-length for the individual frequency limits ranges from 2.13205m to 10.41058m, $L_c = 0.5$m provided a good comparison indicating that L_c does not depend on the length of a regular wave. From these tests the required condition for overlapping zone length in MLPG_RS domain can be concluded as $\frac{L_c}{\Delta r} \geq 10$, where Δr is the initial resolution for particle distribution. The focusing wave results also confirms the implementation of moving side-wall algorithm to obtain the continuous waterline. The algorithm shows the ability to capture the small-amplitude waves necessary for accurately replicating shape, focusing point and phase of the focusing wave group, including the high frequency waves. These results show superior agreement to experiments as compared to similar SPH as shown in [17].

3.3. Experimental setup

The numerical model is validated against experiments conducted on interaction of fixed cylinder with focusing and regular waves. The experiments were performed using the wave tank in the Franzius-Institute Laboratory, Hannover, Germany. The tank is 110.0m long, 2.2m wide, and 2.0m deep with a computer-controlled hydraulically driven piston type wave-maker at one end of the tank and a beach at the other end. The tank was filled with fresh-water to a working depth of 0.7m. The waves were generated using the second order Schaffer correction to suppress the spurious free waves, as described in [32]. Wave probes were placed at location shown in Table (1) for measuring the generated waves. A cylinder of diameter 0.22m is fixed at a distance of 24.88m from the wave-maker, with its centre close to the mid-line of the flume at 1.085m from the side-wall. It is fixed with eight pressure transducers with sampling frequency of 100Hz, five towards the wave-maker at different depths and three around the cylinder as shown in Fig. (19) and their location on the cylinder is described in Table (2). Here, $\alpha = 0°$ is for the pressure probes on the cylinder surface towards the wave-maker. Note that $PP4$ and $PP5$ are placed above the initial water-level.

The details of the regular wave and a focused wave against which the numerical results will be compared are given in Table (3). Here f_c is the central frequency, Δf is the bandwidth, N is the number of frequency components, f_1 is the starting frequency, f_N is the ending frequency, G_a is the gain, t_f is the focusing time and X_f the focusing point. For convenient comparison of numerical and experimental results, the values of length are non-dimensionalised with respect to initial still water depth d_0, time with respect to $t_0 = \sqrt{\frac{d}{g}}$ and pressure with respect to $P_0 = \rho g d_0$. Hence, the location and diameter of the cylinder are $35.5429 d_0$ and
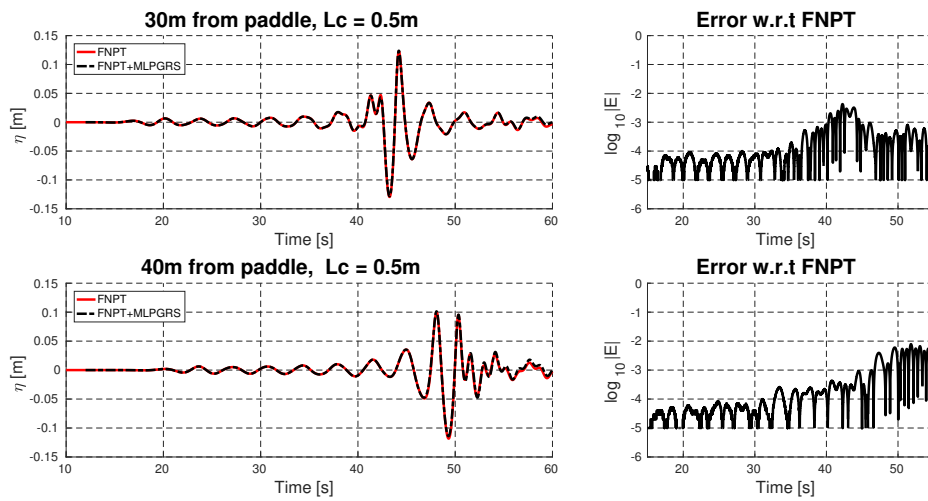
Figure 18: Wave probes comparison of surface elevation η between FNPT results and coupled FNPT+MLPG_RS results with $L_c = 0.5$m for focused wave
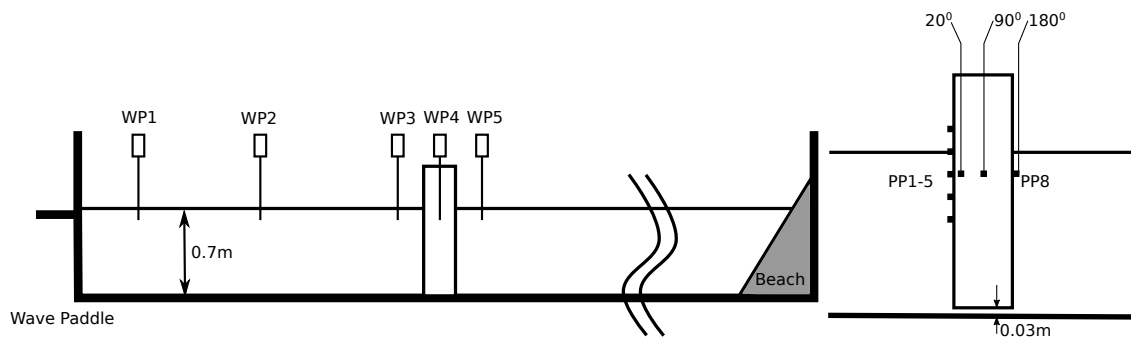

Figure 19: Schematic for physical wave tank and cylinder along with location of probes

$0.3143d_0$ respectively.

3.4. Interaction of fixed cylinder with different waves

The numerical domain is $58.5429d_0$ long, $1.6d_0$ wide with initial water depth $1d_0$. The cylinder of diameter $0.3143d_0$ and height $1.5d_0$ is fixed with its centre at $x = 35.5429d_0$ and $y = 0.8d_0$. The total domain is split between the 2D FNPT sub-domain starting from the wave-maker for wave-generation and propagation, and the 3D MLPG_RS domain starting from $28.5429d_0$. In section 3.2 we have shown the successful transfer of $TW1$ and $TW2$ from the FNPT domain to the MLPG_RS domain, therefore the same 2D mesh characteristics will be used for the FNPT sub-domain, with $\Delta x = 0.0625d_0$ and Δy varying exponentially from $0.1094d_0$ near bottom to $0.0241d_0$ near the free-surface in 20 intervals. The region $R2$ for the FNPT-FEM domain lies from $x = 28d_0$ to $x = 32d_0$ with the length of the overlapping zone fixed to $L_c = 1.0d_0$. These parameters are kept same for all the test cases based on the conclusion from section 3.2.

The MLPG_RS sub-domain is $30d_0$ long, initially starting from $28.5429d_0$, $1.6d_0$ wide with initial water-depth of $1d_0$. A $10d_0$ long sponge layer is placed on the right end to absorb the incoming wave. The initial particle distribution is done as a Cartesian grid with uniform spacing Δr. However, a radial particle distribution is done in the vicinity of the cylinder by placing nodes at regular intervals along the normal of body nodes as shown in Fig. (20). It improves the Lagrangian motion of these fluid particles around the cylinder.

Wave Probe	X Distance from wave-maker X(m)	Y Distance from side-wall Y(m)
WP1	4.9750	1.085
WP2	14.4280	1.085
WP3	24.3100	0.825
WP4	24.8800	0.825
WP5	25.5850	0.825

Table 1: Location of wave-probes in experiment setup

Pressure Probe	Vertical location Z(m)	Non-dimensional $\frac{Z}{d_0}$	Angular position α
PP1	0.4150	0.5929	0°
PP2	0.5150	0.7357	0°
PP3	0.6150	0.8786	0°
PP4	0.7150	1.0214	0°
PP5	0.8150	1.1643	0°
PP6	0.6150	0.8786	20°
PP7	0.6150	0.8786	90°
PP8	0.6150	0.8786	180°

Table 2: Location of pressure-probes on the cylinder in experiment setup

Name -	d (m)	f_c (Hz)	Δf -	N -	f_1 (Hz)	f_N (Hz)	X_f (m)	t_f (s)	G_a -	H (m)
TW1	0.7	0.5	-	-	-	-	-	-	-	0.1
TW2	0.7	0.6857	0.6857	32	0.3429	1.0286	23	38	0.002	-

Table 3: Details of the waves tested for interaction with the cylinder

Name	$\frac{\Delta t}{t_0}$	$\frac{\Delta r}{d_0}$	$\frac{\Delta t \sqrt{g d_0}}{\Delta r}$	Time-steps Total	Time-steps on MLPG_RS	Nodes Fluid
M1T235	0.0235	0.0500	0.4698	7800	6200	416336
M1T251	0.0251	0.0500	0.5011	7312	5812	416336
M1T313	0.0313	0.0500	0.6264	5850	4650	416336
M1T376	0.0376	0.0500	0.7517	4875	3875	416336
M1T392	0.0392	0.0500	0.7830	4680	3720	416336
M1T470	0.0470	0.0500	0.9396	3900	3100	416336
M2T235	0.0235	0.0625	0.3759	7800	6200	220890
M2T251	0.0251	0.0625	0.4009	7312	5812	220890
M2T313	0.0313	0.0625	0.5011	5850	4650	220890
M2T376	0.0376	0.0625	0.6014	4875	3875	220890
M2T392	0.0392	0.0625	0.6264	4680	3720	220890
M2T470	0.0470	0.0625	0.7517	3900	3100	220890
M2T626	0.0626	0.0625	1.0023	2925	2325	220890
M3T313	0.0313	0.0833	0.3759	5850	4650	117384
M3T392	0.0392	0.0833	0.4698	4680	3720	117384
M3T470	0.0470	0.0833	0.5638	3900	3100	117384
M3T626	0.0626	0.0833	0.7517	2925	2325	117384

Table 4: Details of particle distribution and time-step of the numerical setups for focusing wave $TW2$
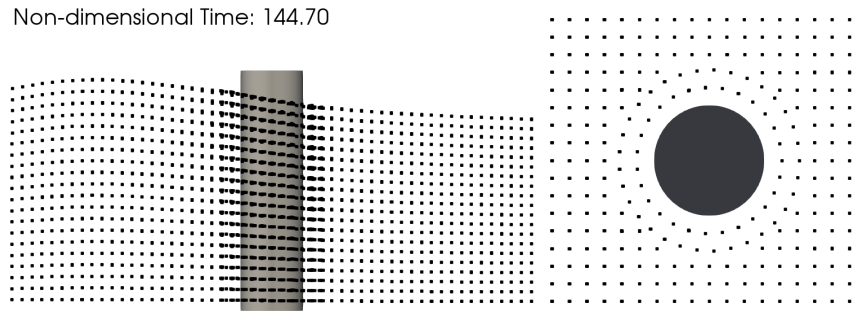
Non-dimensional Time: 144.70

Figure 20: Radial particle distribution in the vicinity of the cylinder

The first test results are presented for the focusing wave $TW2$. Three particle distribution are tested, with the finest being $M1$ with $\Delta r = 0.0500 d_0$, followed by $M2$ with $\Delta r = 0.0625 d_0$ and the coarsest $M3$ with $\Delta r = 0.0833 d_0$. Each of them is tested with time-step ranging from $0.0235 t_0$ to $0.0626 t_0$. The combination of Δr and Δt which were successfully tested are shown in Table (4). The number of nodes listed in this table are only for the MLPG_RS sub-domain. The total simulation time is $183 t_0$ resulting in number of time-steps as shown in Table (4). However, as the MLPG_RS domain starts from $28.5429 d_0$ onwards, there is no need to solve the particle based problem for the first $37.5851 t_0$ till the wave reaches this sub-domain, which directly reduces the computational effort by 21%.

A mesh and time-step convergence study is conducted for the focusing wave $TW2$. Results are compared using pressure probe signals from the experiment and simulations. For the purpose of convergence analysis, error is quantified using root-mean-square of the difference between numerical and experiment pressure. The RMSE plot for $PP2$ and $PP6$ for all of numerical setups from Table (4) are shown in Fig. 21, with similar results for the other pressure probes. In particle based schemes the ratio $\Delta r / \Delta t$ is an important parameter for solution stability and accuracy, and as per [29], it should be kept within the range of $5 - 7$ for MLPG_RS scheme. However, the value being dimensional is difficult to interpret in that form. Therefore, RMSE is plotted against two different x-axis, time-step Δt and ratio $c_t = \Delta t \sqrt{g d_0} / \Delta r$, where c_t is a form of Courant coefficient with characteristic velocity taken as $\sqrt{g d_0}$, similar to the approach taken by established overturning wave work by [40]. Therefore the recommendation from [29] will convert to range of c_t within $0.4 - 0.65$.

It is observed from the RMSE plot that $M3$ results in higher error irrespective of the time-step compared to the fine particle distribution. This can be explained by observing the difference in numerical results using $M3$ and $M2$ with same time-step as shown in Fig. (22). $M3$ results in lower estimation of pressure even before the focusing event. This is due to the coarse MLS gradient. A finer Δr reduces MLS gradient error, as evident from the $M2$ pressure which overlaps with the experiment. $M3$ shows highest errors for troughs, which is highlighted for the steepest trough at $t = 148 t_0$ for $PP3$. Lagrangian motion in trough region spreads the nodes apart. Support domain radius for each node is calculated dynamically to ensure sufficient neighbouring nodes. Therefore this Lagrangian spread of nodes in the trough region results in larger support domain radius, thus lowering the accuracy of gradients. Alternatively, the crest region brings the nodes closer, which helps in maintaining gradient accuracy. For finer resolution such as $M2$, the increase in support domain radius due to Lagrangian spread is not sufficient to reduce gradient accuracy, resulting in better capture of the steepest trough.

A lower time-step reduces error in the numerical form of the differential equation. However, in Lagrangian methods the time-step also plays a crucial role in particle distribution, and hence effects the simulation stability. This is observed by comparing results for $M2$ from two time-steps as shown in Fig. (23). Pressure from both time-steps is similar, but the smaller time-step results in more stable solution. This is because the smaller time-step results in smaller motion of nodes per time-step, and provides particle collision algorithm better opportunity for maintaining particle distribution. A large time-step may momentarily bring two-nodes very close to each other resulting is unnaturally high gradients, seen as noise in pressure results.
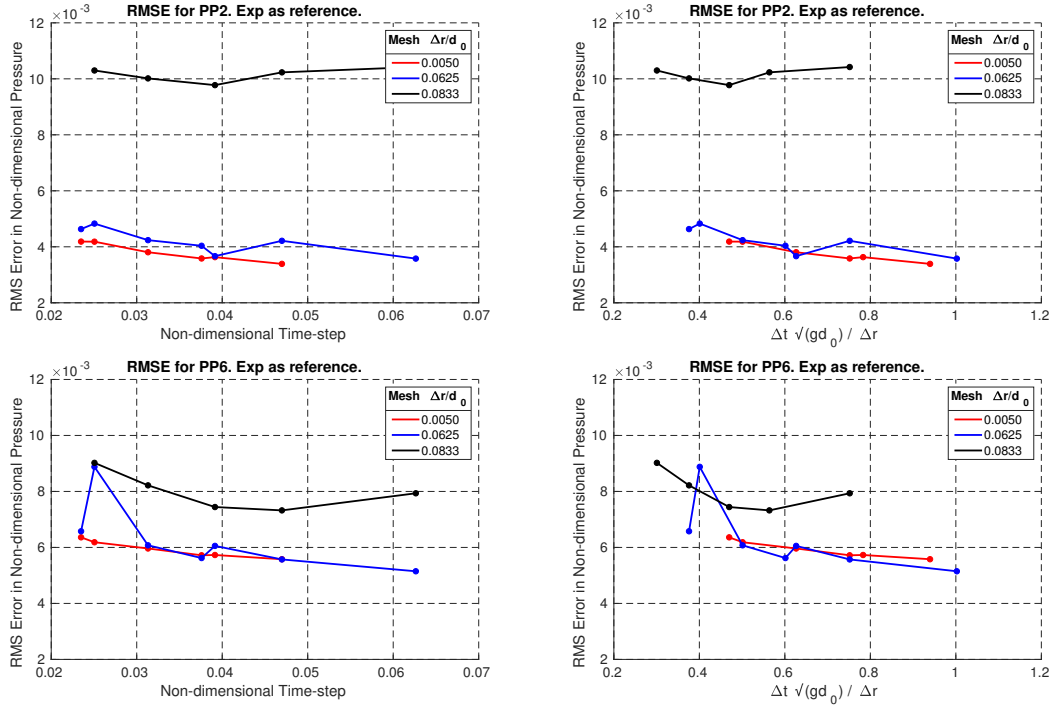
Figure 21: Root-mean-squared error between numerical and experiment pressure for $PP2$ and $PP6$, with time-step and $c_t = \Delta t \sqrt{gd_0}/\Delta r$ as x-axis

However this momentary noise in pressure will not show up in the RMSE value. These momentary high
gradients may sometimes throw particles apart resulting in simulation failure.

From Fig. (21) it is observed that RMSE for $M1$ and $M2$ are similar for almost all setups. We can
observe a small increase in RMSE for the smallest Δt in both $M1$ and $M2$. This is due to introduction of
small phase shift which is exaggerated in the RMSE value. But the RMSE for all time-steps for $M1$ and
$M2$ are in similar range. Therefore it can be concluded that a further reduction in particle distribution will
not further improve accuracy, hence confirming convergence. This is also observed in the Fig. (24), where
the pressure for $M1T235$ and $M2T313$ overlap for all pressure probes.

We also investigate the conservation of mass by the MLPG_RS scheme using the converged setup $M2T313$
for focusing wave case $TW2$. A control volume of length $L_{cv} = 6d_0$, width $B_{cv} = 1.6d_0$ and height $2d_0$
is placed between $x = 32.5429d_0$ and $x = 38.5429d_0$, thus covering the cylinder. The fluid flows in and
out of vertical planes of this control volume. These vertical planes (control surfaces) are discretised in
regular intervals and MLPG_RS solution is interpolated on these vertical planes using MLS. Mass of fluid
inside the control volume is calculated by integrating volume under the free-surface. Conservation of mass
is investigated by monitoring the error in mass flux for this control volume, using Eq. (20). Here the 2D
surface integration is done using Simpson's 9-point scheme and time-derivative is calculated using central
difference method. The error is non-dimensionalised using $E_{nd} = \rho L_{cv} B_{cv} \sqrt{gd_0}$. The non-dimensional error
is observed to be of the order 10^{-3} as reported at every time-step in Fig. (25).

$$E_{cv} = -\frac{\partial m_{cv}}{\partial t} + \iint_{cs} \rho(\vec{u}.\vec{n})dS \tag{20}$$

The setup $M2T313$ is used to simulate the interaction of regular wave $TW1$ with the cylinder. Con-
vergence was demonstrated for setup $M2T313$ for the steep narrow-banded focusing wave $TW2$ and is
expected to show good performance for the lesser steep $TW1$. Results for the pressure probes are presented
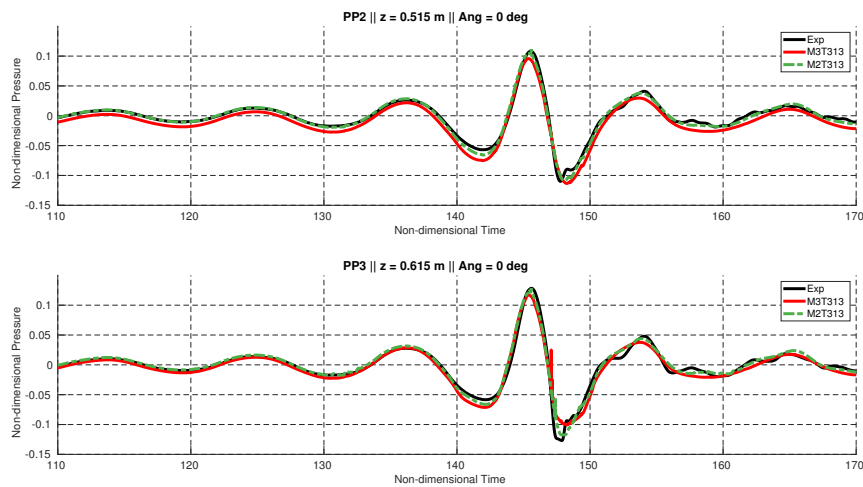
Figure 22: Comparison between experimental and numerical pressure probe for $\Delta r = 0.0833d_0$ and $\Delta r = 0.0625d_0$ with time-step $\Delta t = 0.0313t_0$

in Fig. (27) showing good agreement against the experiments. Please note the excellent comparison for $PP4$ which is located above the initial water level. Estimation of pressure at this location requires accurate capture of the free-surface. This result highlights the strength of MLPG_RS in simulating the free-surface. An Eulerian model for free-surface flow would require a fine mesh in the region of free-surface motion for an accurate capture of free-surface.

Influence of the developments in this model can be seen in Fig. (26) and Fig. (27), where the results for the pressure probes are compared against the previous 3D MLPG_R work based on [23] and [41]. The results from the earlier work for $TW2$ show instances of noise in the simulation with a deviation in phase and amplitude as compared to the experiments. These errors in the earlier work have resulted from the misidentification of free-surface nodes as was shown in Fig. (5), improper particle distribution in the vicinity of the cylinder under the waves and improper application of the rigid-wall BC. The issue is further compounded for regular wave $TW1$, where the structure is exposed to a number of steep waves in succession leading to improper particle distribution and subsequent simulation failure.

A 3D illustration of velocity magnitude in the vicinity of the cylinder under the steepest crest and trough for case $TW2$ is shown in Fig. (28) and Fig. (29) respectively. The developments outline in section 2.3-2.8 result in smooth, non-damping, stable solutions for both $TW1$ and $TW2$. The hybrid approach for wave-making boundary has allowed for reduction of 3D domain by 49% for this problem, with a further reduction of 21% in the number of time-steps.

4. Conclusion

The paper presented a detailed new 3D formulation of the solution procedure for Navier-Stokes equation for incompressible Lagrangian flow problem using MLPG. The existing MLPG_R scheme with it Petrov-Galerkin formulation using Rankine source had the significant advantage of removing gradient operations from the unknown quantity. This paper has additionally provided the derivation of a semi-analytical integration technique with a symmetric expression (MLPG_RS) and has quantified the associated error. A detailed analysis of the influence of the integration domain radius on the stability and accuracy of the solution was conducted to understand the integration method error. Based on this, we have prescribed the radius of the support domain and the integration domain.

A detailed algorithm was presented for coupling of 2D FNPT-FEM with the 3D MLPG_RS method. This hybrid approach was used as the wave-making condition, which limited the need for 3D domain to the vicinity of the cylinder. It allowed us to significantly reduce the 3D computational domain and number of
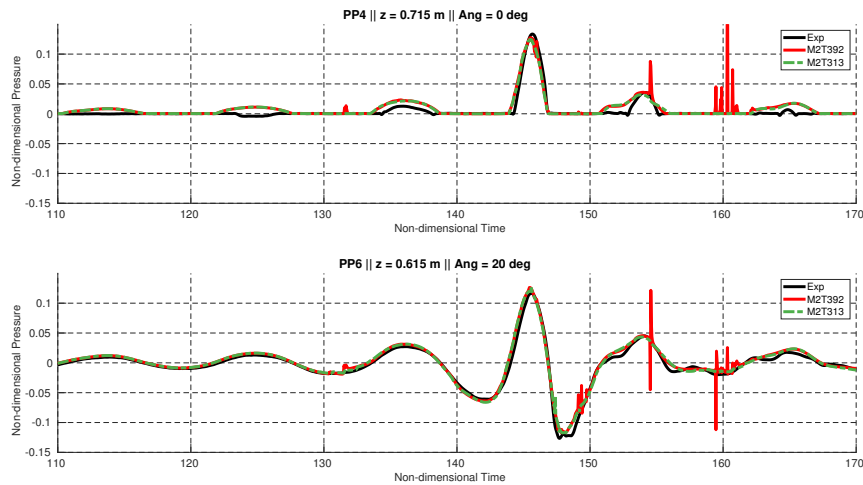
Figure 23: Comparison between experimental and numerical pressure probe for $\Delta r = 0.0625d_0$ with time-step $\Delta t = 0.0392t_0$ and $\Delta t = 0.0313t_0$

time-steps, and has improved the overall computational efficiency of the model. A detailed analysis was done to identify the appropriate size of overlapping zone between the 2D and the 3D domain for solitary, regular and focusing waves. The paper presents minimum overlapping zone length criterion for successful coupling. We were able to use the strength of potential flow model in accurate wave-generation and propagation over long distances, due to which the wave reaching the cylinder was highly accurate and resulted in excellent agreement of numerical pressure probe signals with the experiments.

We have demonstrated the issue of mis-identification of free-surface particles in the vicinity of the cylinder with the existing scheme and have provided a simple alternative technique instead. A moving wall algorithm was presented to capture the waterline on side-wall faces. It enabled the model to capture small amplitude waves and thus made it possible to accurately replicate a focusing wave. We briefed upon the other improvements in application of rigid wall boundary condition, particle collision and redistribution. The collective result of these modifications was demonstrated through pressure probe signal comparison, highlighting the improvements in the accuracy and the stability.

MLPG_RS has the strength of simulating complex flows using relatively lesser number of nodes in comparison to other particle based schemes. This was demonstrated through the mesh and time-step convergence study in this paper. We highlighted the capabilities through excellent comparison of pressure for probes located outside the initial water level. We have also conducted a mesh and time-step convergence study and have demonstrated the suitable range of parameters for interaction of waves with fixed structures. This work has set the basis for further developments in MLPG towards 3D simulation of moving and floating bodies. The hybrid modelling approach will be extended to further reduce the computational domain by shifting the absorbing layer to a potential flow model. Such developments can help bring particle based schemes in the mainframe.

The present manuscript has presented and validated a baseline laminar 3D MLPG model. The complex cases of interaction of cylinder with banded steep focusing wave helped us identify issues with the model which may be hidden under the noise of breaking waves. Therefore, with the confidence in the improvements presented in this manuscripts we will present a detailed study on breaking waves in 3D using MLPG in our future work.
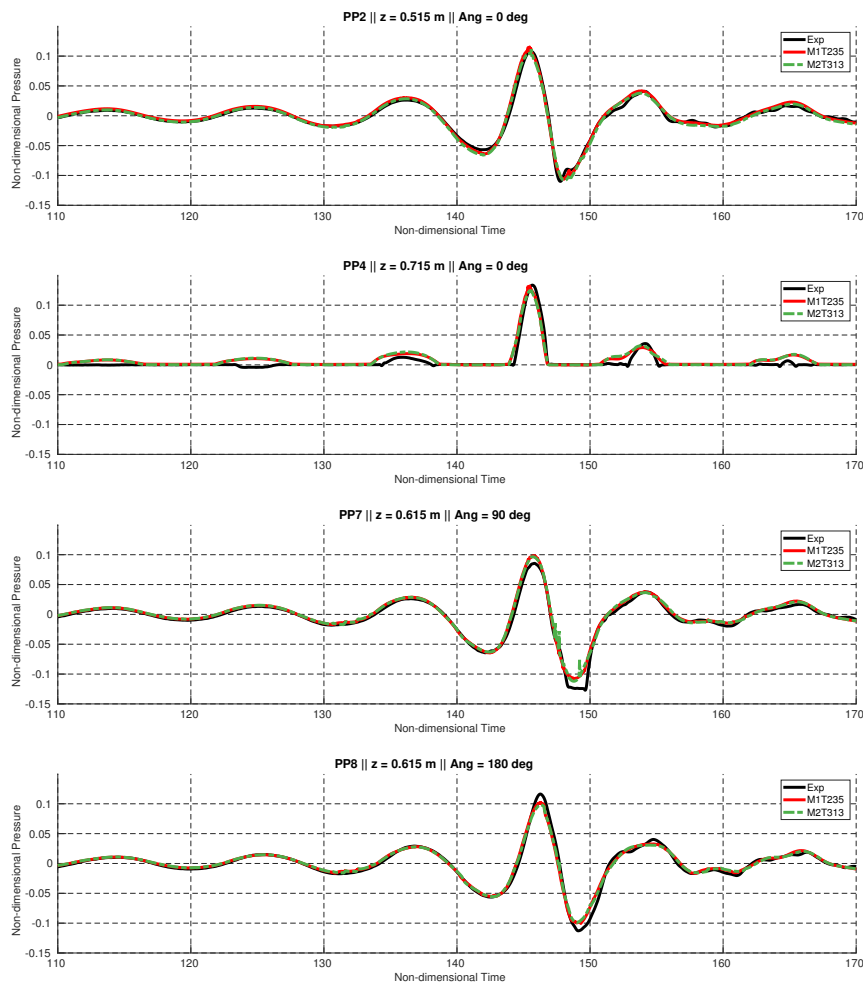
5. Acknowledgement

Figure 24: Comparison between experimental and numerical pressure probe signals for the two best pairs of mesh-time-step combinations

DST-INSPIRE. The application and other developments are part of DST-UKIERI collaboration project with City, University of London.

References

[1] J.-C. Park, M.-H. Kim, H. Miyata, Fully non-linear free-surface simulations by a 3d viscous numerical wave tank, International Journal for Numerical Methods in Fluids 29 (6) (1999) 685–703. `doi:10.1002/(SICI)1097-0363(19990330)29:6<685::AID-FLD807>3.0.CO;2-D`.

[2] P. Higuera, J. L. Lara, I. J. Losada, Realistic wave generation and active wave absorption for navierstokes models: Application to openfoam, Coastal Engineering 71 (2013) 102 – 118. `doi:https://doi.org/10.1016/j.coastaleng.2012.07.002`.

[3] L. Chen, J. Zang, A. Hillis, G. Morgan, A. Plummer, Numerical investigation of wavestructure interaction using openfoam, Ocean Engineering 88 (2014) 91 – 109. `doi:https://doi.org/10.1016/j.oceaneng.2014.06.003`.
    URL `http://www.sciencedirect.com/science/article/pii/S0029801814002169`

[4] S. T. Grilli, P. Guyenne, F. Dias, A fully non-linear model for three-dimensional overturning waves over an arbitrary bottom, International Journal for Numerical Methods in Fluids 35 (7) (2001) 829–867. `doi:10.1002/1097-0363(20010415)35:7<829::AID-FLD115>3.0.CO;2-2`.

[5] P. Guyenne, S. T. Grilli, Numerical study of three-dimensional overturning waves in shallow water, Journal of Fluid Mechanics 547 (2006) 361388. `doi:10.1017/S0022112005007317`.
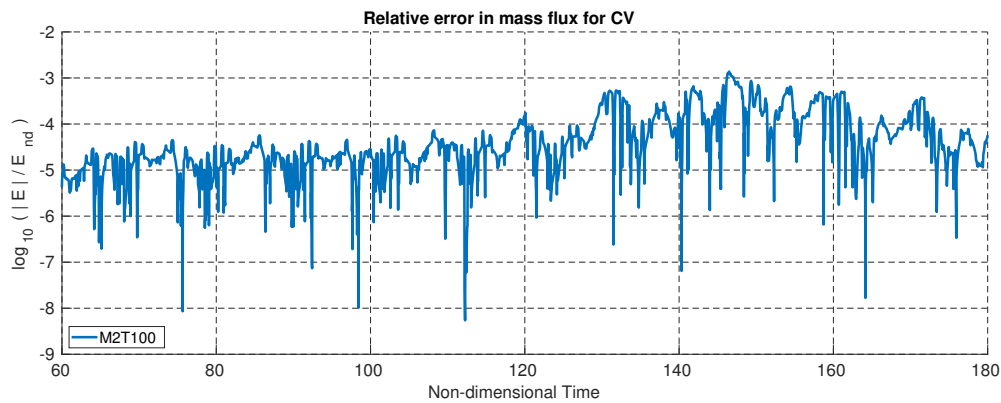
Figure 25: Instantaneous error in mass flux for a control volume encompassing the cylinder, tested for focusing wave $TW2$ for numerical set-up $M2T313$
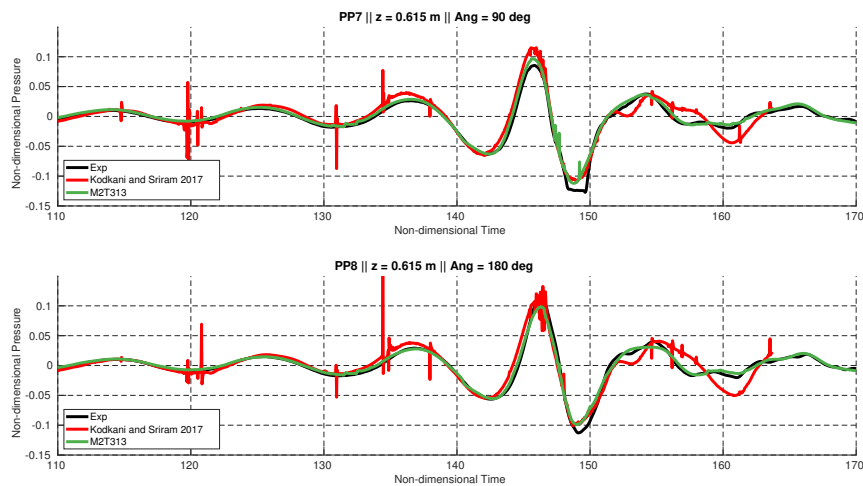

Figure 26: Pressure probe signal for focusing wave $TW2$ compared against the previous MLPG_R work, highlighting the improvements in the current model resulting in stable simulation

[6] Q. W. Ma, S. Yan, Qale-fem for numerical modelling of non-linear interaction between 3d moored floating bodies and steep waves, International Journal for Numerical Methods in Engineering 78 (6) (2009) 713–756. `arXiv:https://onlinelibrary.wiley.com/doi/pdf/10.1002/nme.2505, doi:10.1002/nme.2505`.
URL `https://onlinelibrary.wiley.com/doi/abs/10.1002/nme.2505`

[7] S. Yan, Q. Ma, Qale-fem for modelling 3d overturning waves, International Journal for Numerical Methods in Fluids 63 (6) (2010) 743–768, cited By 31. `doi:10.1002/fld.2100`.

[8] Z. H. Ma, L. Qian, P. J. Martínez-Ferrer, D. M. Causon, C. G. Mingham, W. Bai, An overset mesh based multiphase flow solver for water entry problems, Computers & Fluids 172 (2018) 689–705. `doi:https://doi.org/10.1016/j.compfluid.2018.01.025`.
URL `http://www.sciencedirect.com/science/article/pii/S004579301830032X`

[9] R. Mittal, G. Iaccarino, Immersed boundary methods, Annual Review of Fluid Mechanics 37 (1) (2005) 239–261. `doi:10.1146/annurev.fluid.37.061903.175743`.
URL `https://doi.org/10.1146/annurev.fluid.37.061903.175743`

[10] J. Yang, F. Stern, Sharp interface immersed-boundary/level-set method for wavebody interactions, Journal of Computational Physics 228 (17) (2009) 6590–6616. `doi:https://doi.org/10.1016/j.jcp.2009.05.047`.
URL `http://www.sciencedirect.com/science/article/pii/S0021999109003209`

[11] Z. Xie, T. Stoesser, A three-dimensional Cartesian cut-cell/volume-of-fluid method for two-phase flows with moving bodies, Journal of Computational Physics 416 (2020) 109536. `doi:https://doi.org/10.1016/j.jcp.2020.109536`.
URL `http://www.sciencedirect.com/science/article/pii/S0021999120303107`

[12] P. Lin, A fixed-grid model for simulation of a moving body in free surface flows, Computers & Fluids 36 (3) (2007) 549–561.
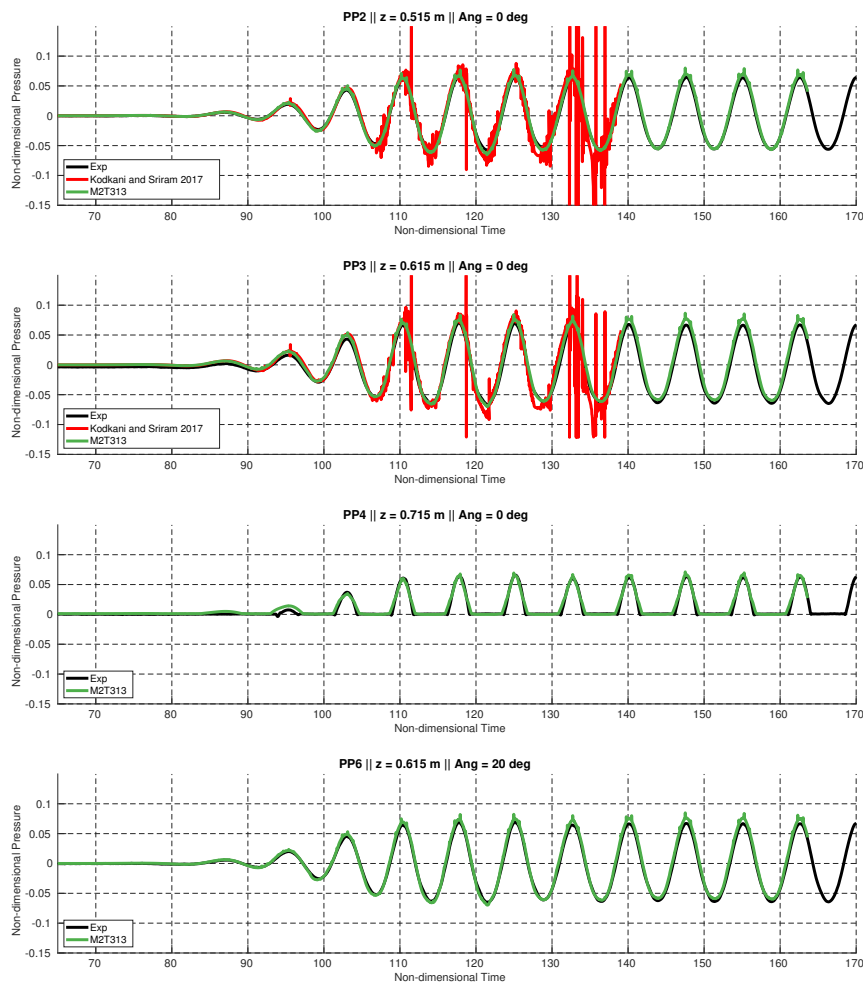
Figure 27: Pressure probe signals for regular wave $TW1$ compared against experiment and previous MLPG_R work, highlighting the improvements in the current model resulting in stable simulation

doi:https://doi.org/10.1016/j.compfluid.2006.03.004.
URL http://www.sciencedirect.com/science/article/pii/S0045793006000570

[13] P. Lin, L. Cheng, D. Liu, A two-phase flow model for wavestructure interaction using a virtual boundary force method, Computers & Fluids 129 (2016) 101–110. doi:https://doi.org/10.1016/j.compfluid.2016.02.007.
URL http://www.sciencedirect.com/science/article/pii/S0045793016300251

[14] Z. Xie, T. Stoesser, S. Yan, Q. Ma, P. Lin, A Cartesian cut-cell based multiphase flow model for large-eddy simulation of three-dimensional wave-structure interaction, Computers & Fluids 213 (2020) 104747. doi:https://doi.org/10.1016/j.compfluid.2020.104747.
URL http://www.sciencedirect.com/science/article/pii/S0045793020303170

[15] N. Nangia, N. A. Patankar, A. P. S. Bhalla, A DLM immersed boundary method based wave-structure interaction solver for high density ratio multiphase flows, Journal of Computational Physics 398 (2019) 108804. doi:https://doi.org/10.1016/j.jcp.2019.07.004.
URL http://www.sciencedirect.com/science/article/pii/S0021999119304887

[16] J. Monaghan, Simulating Free Surface Flows with SPH, Journal of Computational Physics 110 (2) (1994) 399–406. arXiv:arXiv:1011.1669v3, doi:10.1006/jcph.1994.1034.
URL http://linkinghub.elsevier.com/retrieve/pii/S0021999184710345

[17] A. D. Chow, B. D. Rogers, S. J. Lind, P. K. Stansby, Numerical wave basin using incompressible smoothed particle hydrodynamics (ISPH) on a single GPU with vertical cylinder test cases, Computers & Fluids 179 (2019) 543–562. doi:10.1016/j.compfluid.2018.11.022.
URL   https://doi.org/10.1016/j.compfluid.2018.11.022https://linkinghub.elsevier.com/retrieve/pii/
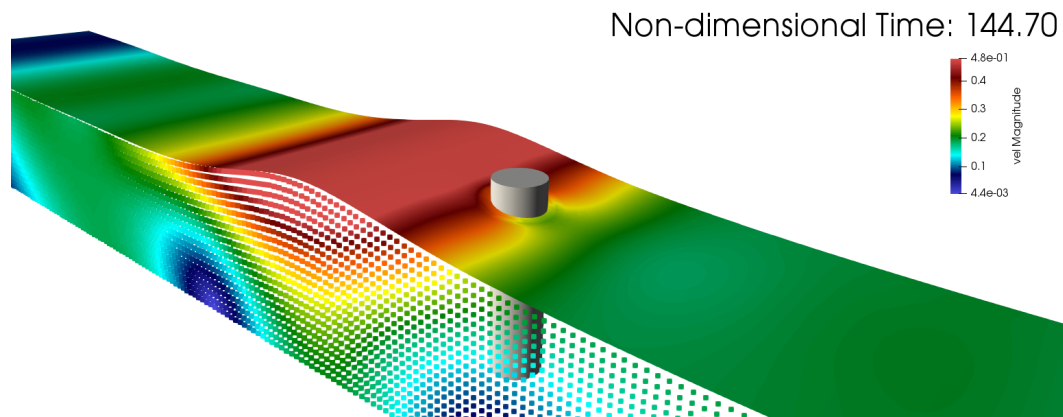
Figure 28: 3D Surface plot for velocity magnitude in the vicinity of the cylinder under the action of the steepest crest in focusing wave $TW2$
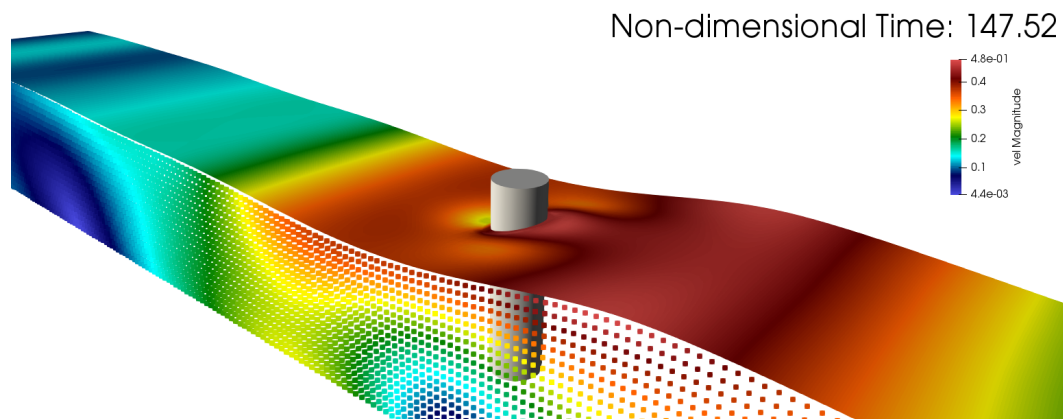

Figure 29: 3D Surface plot for velocity magnitude in the vicinity of the cylinder under the action of the steepest trough in focusing wave $TW2$

S0045793018309034

[18] A. Khayyer, H. Gotoh, Enhancement of stability and accuracy of the moving particle semi-implicit method, Journal of Computational Physics 230 (8) (2011) 3093 – 3118. doi:https://doi.org/10.1016/j.jcp.2011.01.009.
URL http://www.sciencedirect.com/science/article/pii/S0021999111000271

[19] X. Chen, D. Wan, GPU accelerated MPS method for large-scale 3-D violent free surface flows, Ocean Engineering 171 (May 2018) (2019) 677–694. doi:10.1016/j.oceaneng.2018.11.009.
URL https://doi.org/10.1016/j.oceaneng.2018.11.009

[20] S. Idelsohn, E. Oate, F. D. Pin, The particle finite element method: a powerful tool to solve incompressible flows with free-surfaces and breaking waves, International Journal for Numerical Methods in Engineering 61 (7) (2004) 964–989. arXiv:https://onlinelibrary.wiley.com/doi/pdf/10.1002/nme.1096, doi:10.1002/nme.1096.
URL https://onlinelibrary.wiley.com/doi/abs/10.1002/nme.1096

[21] S. N. Atluri, S. Shen, The Meshless Local Petrov-Galerkin (MLPG) method: A simple & less-costly alternative to the finite element and boundary element methods, CMES - Computer Modeling in Engineering and Sciences 3 (1) (2002) 11–51. doi:10.3970/cmes.2002.003.011.

[22] L. Dong, T. Yang, K. Wang, S. N. Atluri, A new Fragile Points Method (FPM) in computational mechanics, based on the concepts of Point Stiffnesses and Numerical Flux Corrections, Engineering Analysis with Boundary Elements 107 (July) (2019) 124–133. doi:10.1016/j.enganabound.2019.07.009.
URL https://doi.org/10.1016/j.enganabound.2019.07.009

[23] J. T. Zhou, Q. W. Ma, MLPG method based on rankine source solution for modelling 3D breaking waves, CMES - Computer Modeling in Engineering and Sciences 56 (2) (2010) 179–210.

[24] V. Sriram, Q. W. Ma, T. Schlurmann, A hybrid method for modelling two dimensional non-breaking and breaking waves, Journal of Computational Physics 272 (2014) 429–454. doi:10.1016/j.jcp.2014.04.030.

[25] A. S. Rijas, V. Sriram, Numerical modelling of forced heaving of mono hull and twin hull in particle method, Ocean

660   Engineering 173 (2019) 197–214. `doi:https://doi.org/10.1016/j.oceaneng.2018.12.066`.
       URL `http://www.sciencedirect.com/science/article pii/S0029801818312769`

[26]   Q. W. Ma, A new meshless interpolation scheme for MLPG_R method, CMES - Computer Modeling in Engineering and
       Sciences 23 (2) (2008) 75–89.

[27]   W. K. Liu, Y. Chen, S. Jun, J. S. Chen, T. Belytschko, C. Pan, R. A. Uras, C. T. Chang, Overview and applications
665   of the reproducing Kernel Particle methods, Archives of Computational Methods in Engineering 3 (1) (1996) 3–80. `doi:`
       `10.1007/BF02736130`.
       URL `http://link.springer.com/10.1007/BF02736130`

[28]   T. Belytschko, Y. Y. Lu, L. Gu, Element-free Galerkin methods, International Journal for Numerical Methods in Engi-
       neering 37 (2) (1994) 229–256. `doi:10.1002/nme.1620370205`.
670   URL `http://doi.wiley.com/10.1002/nme.1620370205`

[29]   Q. W. Ma, J. T. Zhou, MLPG_R Method for Numerical Simulation of 2D Breaking Waves, CMES - Computer Modeling
       in Engineering and Sciences 43 (3) (2009) 277–303. `doi:10.1080/08870440903194015`.

[30]   G. Liu, Y. Gu, An Introduction to Meshfree Methods and Their Programming, Springer-Verlag, Berlin/Heidelberg, 2005.
       `doi:10.1007/1-4020-3468-7`.
675   URL `http://link.springer.com/10.1007/1-4020-3468-7`

[31]   P. Labs, Paralution v1.0.0 (2015).
       URL `http://www.paralution.com/`

[32]   V. Sriram, T. Schlurmann, S. Schimmels, Focused wave evolution using linear and second order wavemaker theory,
       Applied Ocean Research 53 (2015) 279–296. `doi:10.1016/j.apor.2015.09.007`.
680   URL   `http://dx.doi.org/10.1016/j.apor.2015.09.007https://linkinghub.elsevier.com/retrieve/pii/`
       `S0141118715001212`

[33]   H. A. Schäffer, Second-order wavemaker theory for irregular waves, Ocean Engineering 23 (1) (1996) 47–88. `doi:https:`
       `//doi.org/10.1016/0029-8018(95)00013-B`.
       URL `http://www.sciencedirect.com/science/article/pii/002980189500013B`

685 [34]   V. Sriram, S. A. Sannasiraj, V. Sundar, A. Schlenkhoff, T. Schlurmann, Quantification of phase shift in the simulation of
       shallow water waves, International Journal for Numerical Methods in Fluids`doi:10.1002/fld.2072`.

[35]   H. Gotoh, T. Sakai, Key issues in the particle method for computation of wave breaking, Coastal Engineering 53 (2) (2006)
       171–179. `doi:https://doi.org/10.1016/j.coastaleng.2005.10.007`.
       URL `http://www.sciencedirect.com/science/article/pii/S037838390500133X`

690 [36]   A. Khayyer, H. Gotoh, Y. Shimizu, Comparative study on accuracy and conservation properties of two particle regular-
       ization schemes and proposal of an optimized particle shifting scheme in ISPH context, Journal of Computational Physics
       332 (2017) 236–256. `doi:10.1016/j.jcp.2016.12.005`.
       URL `http://dx.doi.org/10.1016/j.jcp.2016.12.005`

[37]   A. Kruisbrink, S. Korzilius, F. Pearce, H. Morvan, SPH Particle Collisions for the Reduction of Particle Clustering,
695   Interface Stabilisation and Wall Modelling, Journal of Applied Mathematics and Physics 06 (09) (2018) 1860–1882. `doi:`
       `10.4236/jamp.2018.69158`.
       URL `http://www.scirp.org/journal/doi.aspx?DOI=10.4236/jamp.2018.69158`

[38]   A. Chaniotis, D. Poulikakos, P. Koumoutsakos, Remeshed smoothed particle hydrodynamics for the simulation of viscous
       and heat conducting flows, Journal of Computational Physics 182 (1) (2002) 67 – 90. `doi:https://doi.org/10.1006/`
700   `jcph.2002.7152`.
       URL `http://www.sciencedirect.com/science/article/pii/S0021999102971524`

[39]   C. Altomare, J. Domnguez, A. Crespo, J. Gonzlez-Cao, T. Suzuki, M. Gmez-Gesteira, P. Troch, Long-crested wave
       generation and absorption for sph-based dualsphysics model, Coastal Engineering 127 (2017) 37 – 54. `doi:https://doi.`
       `org/10.1016/j.coastaleng.2017.06.004`.
705   URL `http://www.sciencedirect.com/science/article/pii/S0378383916301831`

[40]   S. Yan, Q. W. Ma, QALE-FEM for modelling 3D overturning waves, International Journal for Numerical Methods in
       Fluids 65 (October 2010). `doi:10.1002/fld.2100`.
       URL `http://doi.wiley.com/10.1002/fld.2100`

[41]   A. G. Kodkani, V. Sriram, Numerical study of wave interaction with the vertical cylinder using 3D viscous numerical wave
710   tank, Proceedings of the International Offshore and Polar Engineering Conference 29 (2017) 476–482.